

Small scale behavior of the physical conditions and the abundance discrepancy in the Orion nebula¹

Adal Mesa-Delgado, César Esteban, and Jorge García-Rojas²

Instituto de Astrofísica de Canarias, E-38200 La Laguna, Tenerife, Spain

amd@ll.iac.es, cel@ll.iac.es, jogarcia@ll.iac.es

ABSTRACT

We present results of long-slit spectroscopy in several positions of the Orion nebula. Our goal is to study the spatial distribution of a large number of nebular quantities, including line fluxes, physical conditions and ionic abundances at a spatial resolution of about $1''$. In particular, we have compared the O^{++} abundance determined from collisionally excited and recombination lines in 671 individual 1D spectra covering different morphological zones of the nebula. We find that protoplanetary disks (proplyds) show prominent spikes of $T_e([N\ II])$ probably produced by collisional deexcitation due to the high electron densities found in these objects. Herbig-Haro objects show also relatively high $T_e([N\ II])$ but probably produced by local heating due to shocks. We also find that the spatial distribution of pure recombination $O\ II$ and $[O\ III]$ lines is fairly similar, in contrast to that observed in planetary nebulae. The abundance discrepancy factor (ADF) of O^{++} remains rather constant along the slit positions, except in some particular small areas of the nebula where this quantity reaches somewhat higher values, in particular at the location of the most conspicuous Herbig-Haro objects: HH 202, HH 203, and HH 204. There is also an apparent slight increase of the ADF in the inner $40''$ around θ^1 Ori C. We find a negative radial gradient of $T_e([O\ III])$ and $T_e([N\ II])$ in the nebula based on the projected distance from θ^1 Ori C. We explore the behavior of the ADF of O^{++} with respect to other nebular quantities, finding that it seems to increase very slightly with the electron temperature. Finally, we estimate the value of the mean-square electron temperature fluctuation, the so-called t^2 parameter. Our results indicate that the hypothetical thermal inhomogeneities –if they exist– should be smaller than our spatial resolution element.

Subject headings: ISM: abundances –H II regions– ISM: individual: Orion nebula

²Present address: Instituto de Astronomía, UNAM, Apdo. Postal 70-264, 04510 México D.F., Mexico

1. Introduction

The analysis of the spectrum of H II regions allows to determine the chemical composition of the ionized gas phase of the interstellar medium from the Solar Neighbourhood to the high-redshift Universe. Therefore, it stands as an essential tool for our knowledge of the chemical evolution of the Universe. In photoionized nebulae, the abundance of the elements heavier than He is usually determined from collisional excitation lines (hereinafter CELs), whose intensity depends exponentially on the electron temperature, T_e , of the gas. It was about 20 years ago when the first determinations of C^{++} abundance from the intensity of the weak recombination line (hereinafter RL) of C II 4267 Å were available for planetary nebulae (PNe). The comparison of the abundance obtained from C II 4267 Å and from the CELs of this ion in the ultraviolet (UV) showed a difference that could be as large as a order of magnitude in some objects (e.g. French 1983; Rola & Stasińska 1994; Mathis & Liu 1999). Peimbert et al. (1993) were the first in determining the O^{++} abundance from the very weak RLs, obtaining the same qualitative result: the abundances obtained from RLs are higher than those determined making use of CELs. This observational fact is currently known as the “abundance discrepancy” (hereinafter AD) problem. In the last years, our group has obtained a large dataset of intermediate and high resolution spectroscopy of Galactic and extragalactic H II regions using medium and large aperture telescopes (Esteban et al. 2002, 2005; García-Rojas et al. 2004, 2005, 2006, 2007; López-Sánchez et al. 2007). The general result of these works is that the O^{++}/H^+ ratio calculated from RLs is between 0.10 and 0.35 dex higher than the value obtained from CELs in the same objects. The value of the AD that we usually find in H II regions is rather similar for all objects and ions and is much lower than the most extreme values found in PNe. The results for H II regions obtained by our group are fairly different than those found for PNe, and seem to be consistent with the predictions of the temperature fluctuations paradigm formulated by Peimbert (1967), as it is argued in García-Rojas (2006) and García-Rojas & Esteban (2007). In the presence of temperature fluctuations (parametrized by the mean square of the spatial variations of temperature, the so-called t^2 parameter) the AD can be naturally explained because the different temperature dependence of the intensity of RLs and CELs. The existence and the origin of temperature fluctuations are still controversial problems and a challenge for our understanding of ionized nebulae. Recently, Tsamis & Péquignot (2005) and Stasińska et al. (2007) have proposed an hypothesis to the origin of the AD, which is based on the presence of cold high-metallicity clumps of supernova ejecta still not mixed with the ambient gas of the H II regions. This

¹Based on observations made with the 4.2m William Herschel Telescope (WHT) operated on the island of La Palma by the Isaac Newton Group in the Spanish Observatorio del Roque de los Muchachos of the Instituto de Astrofísica de Canarias.

cold gas would produce most of the emission of the RLs whereas the ambient gas of normal abundances would emit most of the intensity of CELs.

Our group is interested in exploring on what variable or physical process the AD depends from different approaches. One of the most promising is based on the study of the behaviour of this magnitude at small spatial scales, something that has still not been explored in depth in nearby bright Galactic H II regions. In this paper, we make use of deep intermediate-resolution long-slit spectroscopy of the Orion nebula to study the dependence of the AD with respect to different nebular parameters: electron temperature and density, local ionization state of the gas, presence of high velocity material, and its correlation with different morphological structures (proplyds, ionization fronts, globules, Herbig-Haro objects), in H II regions.

The spatial distribution of the physical conditions in the Orion nebula has been investigated by several authors. Baldwin et al. (1991) obtained the density and temperature distribution in 21 and 14 points, respectively, along a $5'$ line west of θ^1 Ori C, finding a density gradient that decreases to the outskirts of the nebula and a constant T_e . Walter et al. (1992) determined electron densities and temperatures and chemical abundances for 22 regions of the Orion nebula. Using also data from the literature, these authors find radial gradients of the physical conditions, but with a positive slope in the case of the temperature determined from [O III] lines. Pogge et al. (1992) obtained Fabry-Perot images of the inner $6'$ of the nebula covering several bright CELs and taken with an average seeing of about $1''.8$. Those authors present a density map obtained from the ratio of the [S II] doublet confirming the presence of a density gradient that reaches its highest point immediately south-southwest of the Trapezium stars, and some localized density enhancements in the Orion bar and some Herbig-Haro objects. Very recently, Sánchez et al. (2007) have obtained an integral field spectroscopy mosaic of an area of $5' \times 6'$ of the center of the Orion nebula, with a spatial resolution of $2''.7$. The electron density map they obtain is consistent with that obtained by Pogge et al. (1992) but richer in substructures, some of them possibly associated to Herbig-Haro objects. Sánchez et al. (2007) also obtain a electron temperature map (derived from the line ratio of [N II] lines) that shows clear spatial variations, which rise near the Trapezium and drop to the outer zones of the nebula. However, an important drawback of the temperature map of Sánchez et al. is that is based on non-flux calibrated spectra and possible effects due to variations in the dust extinction distribution cannot be disregarded. O'Dell et al. (2003) obtained a high spatial resolution map of the electron temperature –derived from the line ratio of [O III] lines– of a $160'' \times 160''$ field centered at the southwest of the Trapezium. The data were obtained from narrow-band images taken with the WFPC of the *HST*. Although they do not find a substantial radial gradient of T_e in the nebula, O'Dell et al. (2003) report the existence of small-scale temperature variations down to a few arcseconds com-

patible with the values of the temperature fluctuations parameter calculated from the AD determinations by Esteban et al. (2004). Rubin et al. (2003) obtained *HST*/STIS long-slit spectroscopy at several slit positions on the Orion nebula analysing the electron temperature and density spatial profiles with resolution elements of $0''.5 \times 0''.5$. These last authors do not find large-scale gradients of the physical conditions along the slits but a relatively large point-to-point variation and some correlation of such variations with several small-scale structures.

The spatial mapping of the AD factor has been performed in few ionized nebulae but largely for PNe. Liu et al. (2000), Garnett & Dinerstein (2001), and Krabbe & Copetti (2006) have found significant differences in the spatial profiles of the O^{++}/H^+ ratio derived making use of RLs and CELs suggesting the presence of chemical inhomogeneities or additional mechanisms for producing the O II lines in these objects. Tsamis et al. (2003) have performed the only available study so far of the spatial distribution of the AD factor in an H II region: 30 Doradus. However, considering the extragalactic nature of this object and the spatial sampling of $3''.5$ used by those authors, their final spatial resolution is very low –about 1pc. In any case, Tsamis et al. (2003) find a rather constant AD factor along the zone covered with their observations, a quite different behavior than that observed in PNe.

In §§ 2 and 3 of this paper we describe the observations, the data reduction procedure and the aperture extraction and measurement of the emission lines. In § 4 we derive the physical conditions and the ionic abundances from both kinds of lines: CELs and RLs. In § 5 we present and discuss the spatial profiles of the physical conditions, line fluxes, and the abundance discrepancy factor along the slit positions. In § 6 we discuss the large-scale radial distribution of some nebular properties along the nebula. In § 7 we explore possible correlations between the AD and different nebular parameters. In § 8 we address and estimate the possible temperature fluctuations inside the nebula. Finally, in § 9 we summarize our main conclusions.

2. Observations, Data Reduction, and Extraction of 1D Spectra

Intermediate-resolution spectroscopy was obtained in 2002 December 27 with the ISIS spectrograph at the 4.2m William Herschel Telescope (WHT) in Observatorio del Roque de los Muchachos (La Palma, Spain). Two different CCDs were used at the blue and red arms of the spectrograph: an EEV CCD with a configuration 4096×2048 pixels with a size of $13.5 \mu\text{m}$ per pixel in the blue arm and a Marconi CCD with 4700×2148 pixels with a pixel size of $13.5 \mu\text{m}$ in the red arm. The dichroic prism used to separate the blue and red beams was set at 5400 \AA . The slit was $3''.7$ long and $1''.03$ wide. Two gratings were used, the R1200B

in the blue arm and the R316R in the red arm. These gratings give reciprocal dispersions of 17 and 62 Å mm⁻¹, and effective spectral resolutions of 0.86 and 3.81 Å for the blue and red arms, respectively. The blue spectra cover from $\lambda\lambda$ 4198 to 5048 Å and the red ones from $\lambda\lambda$ 5370 to 8690 Å. The spatial scale is 0".20 pixel⁻¹ in both arms. The average seeing during the observations was \sim 1".2.

We observed 5 slit positions covering different zones of the nebula and different position angles (see Figure 1). These positions were chosen in order to cover different morphological structures as proplyds (158-323, 158-326, 159-350, 170-337, and 177-341), Herbig-Haro objects (HH 202, HH 203, HH 204, HH 529, and HH 530) and the Orion bar. Due to the high surface brightness of the nebula, a large number of individual short exposures were taken in each slit position and spectral range in order to achieve a good signal-to-noise ratio in the faint C II and O II RLs and to avoid saturation of the brightest emission lines. The journal of observations can be found in Table 1. Note that the 5 slit positions are numbered as 1, 3, 4, 5, and 6, actually there was not a slit position number 2.

The spectra were wavelength calibrated with a CuNe+CuAr lamp. The correction for atmospheric extinction was performed using the average curve for continuous atmospheric extinction at Roque de los Muchachos Observatory. The absolute flux calibration was achieved by observations of the standard stars Feige 15, Feige 110, H600, and Hz 44. All the CCD frames were reduced using the standard *IRAF*³ TWODSPEC reduction package to perform bias correction, flat-fielding, cosmic-ray rejection, wavelength and flux calibration, and sky subtraction.

The extraction of 1D spectra was done automatically through an *IRAF* script, using the *apall* task. First, we traced the apertures interactively by selecting the brightest object (star, proplyd or Herbig-Haro object) in each 2D spectrum. In all cases we adjusted a third-order spline function and obtained a typical *rms* of the fit between 0.05 and 0.1 pixels. In the following step, we defined the apertures to extract for each 2D spectra by using the coefficients obtained in the aperture tracing. For all the slit positions, we extracted apertures of 6 pixels size in the spatial direction, that corresponds to an angular scale of 1".2 –the average seeing during the night. Therefore, each aperture covers a size of 1".2 \times 1".03 in the spatial and spectral directions respectively. At the distance of the Orion nebula (450 pc, O'Dell 2001), 1" corresponds to a linear size of 0.0022 pc, 6.8×10^{-15} cm, or 450 A.U. The slit center in the red arm is some pixels displaced with respect to the slit center in the blue arm; this effect has been corrected in the extraction procedure, ensuring the same spatial

³IRAF is distributed by National Optical Astronomical Observatories, operated by the Associated Universities for Research in Astronomy, Inc., under contract to the National Science Foundation

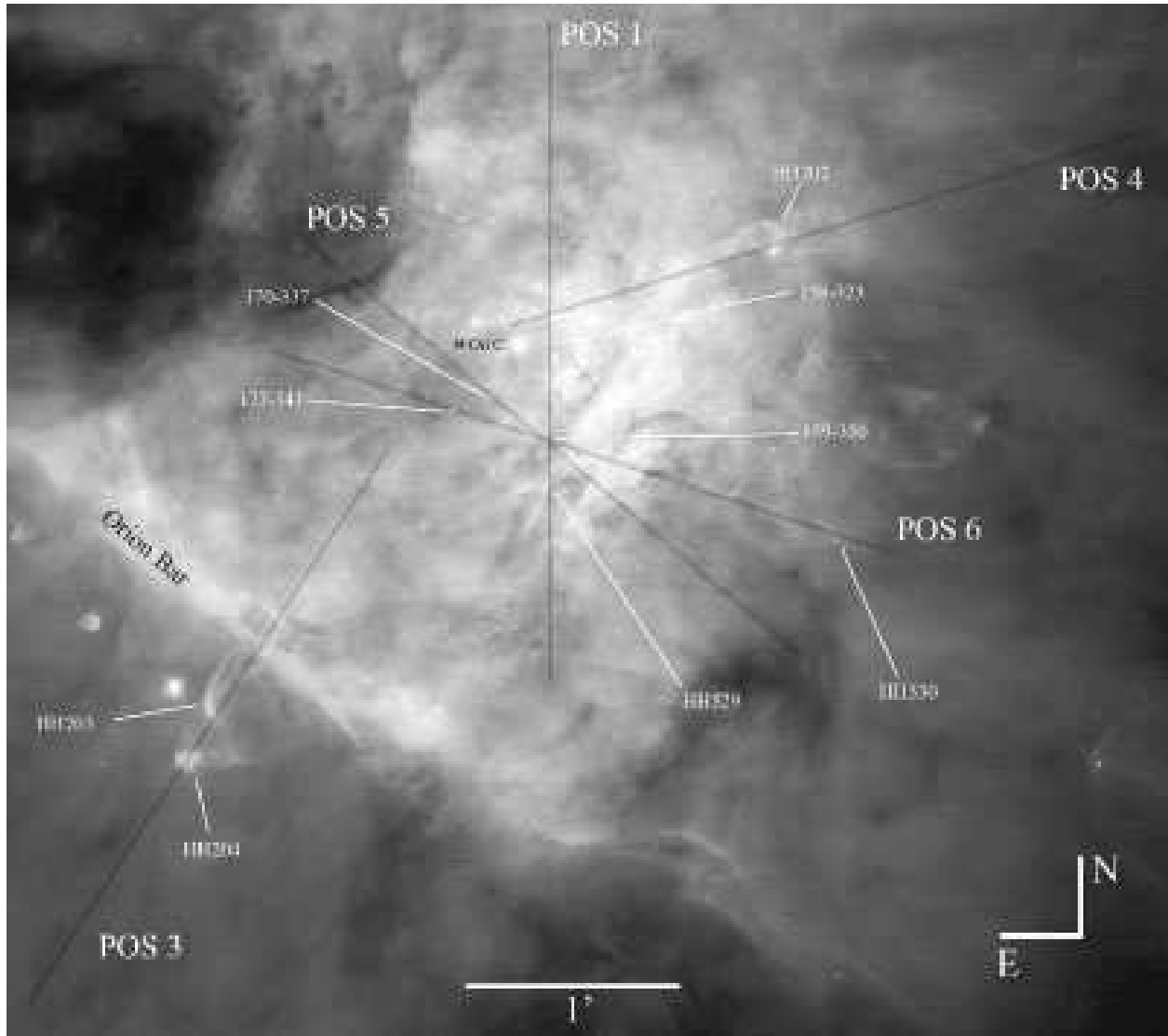


Fig. 1.— Our slit positions over a mosaic of a combination of WFPC2 images of the Orion nebula taken with different filters (O'Dell & Wong 1996).

covering in the blue and red ranges. We have discarded the apertures located near the edges of the CCD, resulting in a final number of 154 apertures extracted –individual 1D spectra– for each slit position except numbers 1 and 4. In these two cases a star – θ^1 Ori A– fell into the slit, and we discarded the apertures contaminated by stellar emission (11 apertures in position 1 and 12 in position 4). In addition, the last 17 apertures at the northwest edge of position 4 were also discarded because the temperature sensitive [O III] 4363 Å line was not detected due to the faintness of the spectra. The final total number of apertures extracted was 730.

For each slit position, we extracted additional 1D spectra collapsing the whole slit –the whole extension of the 154 individual apertures– but excluding different particular zones: a) only those apertures contaminated by stellar emission –these will be designated as “whole slit” spectra, or b) the same zones as in a) but also those apertures covering proplyds, Herbig-Haro objects, or having a very low surface brightness –these spectra are designated as “background gas”. In Table 2, for each slit position, we summarize the number of apertures excluded due to stellar emission contamination or non detection of the [O III] 4363 Å line (upper row), the total number of usable apertures (middle row), and the apertures that we consider representative of the “background gas” (lower row).

3. Emission Line Selection, Flux Measurements, and Reddening Correction

The emission lines considered in our analysis are indicated in Table 3. These lines were selected according to the following criteria:

- H I lines – $H\alpha$, $H\beta$ and $H\gamma$ –, which are used to compute the reddening correction and to re-scale the line intensity ratios of the red spectral range with respect to the blue one.
- Ratios of CELs of various species, which are used to compute physical conditions –such as the auroral lines [O III] 4363 Å or [N II] 5754 Å to derive T_e or [S II] lines to derive n_e – and ionic abundances.
- Faint recombination lines of C II and O II, which are used to derive the C^{++} and O^{++} abundances and to compute the abundance discrepancy factor for O^{++} (via a comparison with the O^{++} abundances from CELs).
- Some lines which are blended with other lines of interest.

Table 1. Journal of observations

Slit Position	R.A. ^a	Decl. ^a	P.A. (deg)	$\Delta\lambda$ (Å)	Spectral Resolution (Å pix ⁻¹)	Exposure Time (s)
1	05 35 15.0	−05 23 04	0	4198–5048 5370–8690	0.23 0.84	30×60 40×30
3	05 35 22.4	−05 25 09	147	4198–5048 5370–8690	0.23 0.84	15×150 25×60
4	05 35 12.4	−05 22 44	107	4198–5048 5370–8690	0.23 0.84	31×60 40×30
5	05 35 15.8	−05 23 33	50	4198–5048 5370–8690	0.23 0.84	20×100 39×30
6	05 35 15.3	−05 23 38	72	4198–5048 5370–8690	0.23 0.84	20×100 41×30

^aCoordinates of the slit center

Table 2. Number of apertures extracted

	Pos 1	Pos 3	Pos 4	Pos 5	Pos 6
No. of excluded apertures ^a	11	...	29
No. of extracted apertures ^b	143	154	125	154	154
“Background gas” zones ^c	1-60,72-84,90-143	85-154	25-50,75-85	1-57,62-74,79,154	1-40,45-63,70-154

^aContaminated by stellar emission or non detection of the [O III] 4363 Å line.

^bSummed for producing the “whole slit” spectra.

^cSummed for producing the “background gas” spectra.

Line fluxes were measured applying a single or a multiple –in the case of line blending– Gaussian profile fit procedure except in some apertures of positions 3 and 4 where the complex velocity field of the Herbig-Haro objects affects the line profiles and the Gaussian fit was not feasible. In these cases, the line intensities were measured by integrating all the flux included in the line profile between two given limits and over a local continuum estimated by eye. All the measurements were made with the SPLOT routine of the *IRAF* package and using our own scripts to automatize the process.

To accurately compute the line fluxes we need to define the adjacent continuum of each line. This was done also by using the SPLOT routine. For each selected line, we define two small spectral zones –one at each side of the line– and located as close as possible of the line and free of any spectral feature. SPLOT fits the continuum between both zones and obtains the flux of the line. This automatic procedure was tested in randomly selected lines where we manually measured the flux using a local continuum estimated by eye. In general, there is a good agreement between both kinds of measurements within the adopted uncertainties. The observational errors associated with the line flux measurements was determined following Castellanos et al. (2002) from the expression $\sigma_1 = \sigma_c N^{1/2} [1 + EW/(N\Delta)]^{1/2}$, where σ_1 is the error in the line flux, σ_c represents the standard deviation of the continuum close to the measured emission line, N is the number of pixels used in the measurement of the line flux, EW is the line equivalent width, and Δ is the wavelength dispersion in \AA pixel^{-1} . The final uncertainty of the line intensity ratios are estimated to be typically: about 1% if the ratio $F(\lambda)/F(\text{H}\beta) \geq 0.1$, about 2% if $0.01 \leq F(\lambda)/F(\text{H}\beta) \leq 0.1$, about 10% if $0.005 \leq F(\lambda)/F(\text{H}\beta) \leq 0.01$, about 25% if $0.001 \leq F(\lambda)/F(\text{H}\beta) \leq 0.005$ and about 40% if $0.0001 \leq F(\lambda)/F(\text{H}\beta) \leq 0.001$. We do not consider lines weaker than $0.0001 \times F(\text{H}\beta)$ (see below).

All the line intensities of a given aperture have been normalized to a particular H I recombination line present in each wavelength interval. For the blue spectra, the reference line was $\text{H}\beta$, and for the red one, the reference was $\text{H}\alpha$. To produce a final homogeneous set of line intensity ratios, all of them were re-scaled to $\text{H}\beta$. The re-scaling factor used in the red spectra was the theoretical $\text{H}\alpha/\text{H}\beta$ ratio for the physical conditions of $T_e = 10000$ K and $n_e = 1000 \text{ cm}^{-3}$.

As it can be expected, weak lines were not detected in all the apertures. To avoid bad weak line measurements, we imposed three criteria to discriminate between real features and noise. The criteria are the following:

- Line intensity peak over 2.5 times the sigma of the continuum (2.5σ): The more usual criterion of 3σ was not adopted because several important lines clearly detected were discarded using that constraint.

- $\text{FWHM}(\lambda) > 1.5 \times \text{FWHM}(\text{H I})$ or $\text{FWHM}(\lambda) < \text{FWHM}(\text{H I})/1.5$: These inequalities were used to discriminate between true emission lines and spurious features.
- $I(\lambda) < 0.0001 \times I(\text{H}\beta)$. This intensity was near the detection limit of our observations.

The reddening coefficient, $c(\text{H}\beta)$, was obtained by fitting the observed $\text{H}\gamma/\text{H}\beta$ ratio to the theoretical one predicted by Storey & Hummer (1995) for the nebular conditions determined in the slit position observed by Esteban et al. (2004). Following Esteban et al. (1998) we have used the reddening function, $f(\lambda)$, normalized at $\text{H}\beta$ derived by Costero & Peimbert (1970) for the Orion nebula. In Figure 2, as an example, we show the spatial distribution of $c(\text{H}\beta)$ obtained for the apertures of the slit position 6. The zone of the largest reddening at the left half of Figure 2 corresponds to the northeast portion of slit position 6. The reddening maps of O’Dell & Yusef-Zadeh (2000) and Sánchez et al. (2007) also show larger values at this zone, which is in the vicinity of the so-called Dark Bay. The typical uncertainty of $c(\text{H}\beta)$ is estimated to be about 0.05.

4. Physical Conditions and Chemical Abundances

4.1. Electron Temperatures and Densities

Nebular electron temperatures, T_e , and densities, n_e , have been derived from the usual CEL ratios, using the IRAF task *temden* of the package *nebular* (Shaw & Dufour 1995) with updated atomic data (see García-Rojas et al. 2005). We have computed n_e from the $[\text{S II}]$ 6717/6731 line ratio and T_e from the nebular to auroral $[\text{O III}]$ (4959+5007)/4363 and $[\text{N II}]$ (6548+6584)/5754 line ratios. The spatial distributions of the physical conditions are presented and discussed in §5.1. Although we include the $[\text{Cl III}]$ doublet in our set of selected lines we do not use the lines in the analysis because the number of apertures with good determinations of the density sensitive line ratio is rather low.

The methodology for the determination of the physical conditions was the following: an initial T_e of 10000 K was assumed in order to derive a first approximation to $n_e([\text{S II}])$; then, the obtained n_e was used to compute $T_e([\text{O III}])$ and $T_e([\text{N II}])$, and finally we iterated until convergence to compute the finally adopted values of n_e and T_e . Uncertainties in the physical conditions were computed by propagating the errors in the analytical expression of n_e computed by Castañeda et al. (1992) and that of T_e given by Osterbrock & Ferland (2006) (their equations 5.4 and 5.5). Although the expression derived by Castañeda et al. (1992) is only valid to a limited range of densities lower than 10^4 cm^{-3} , it seems adequate for simply estimating the error propagation due to uncertainties in the computed temperatures and line

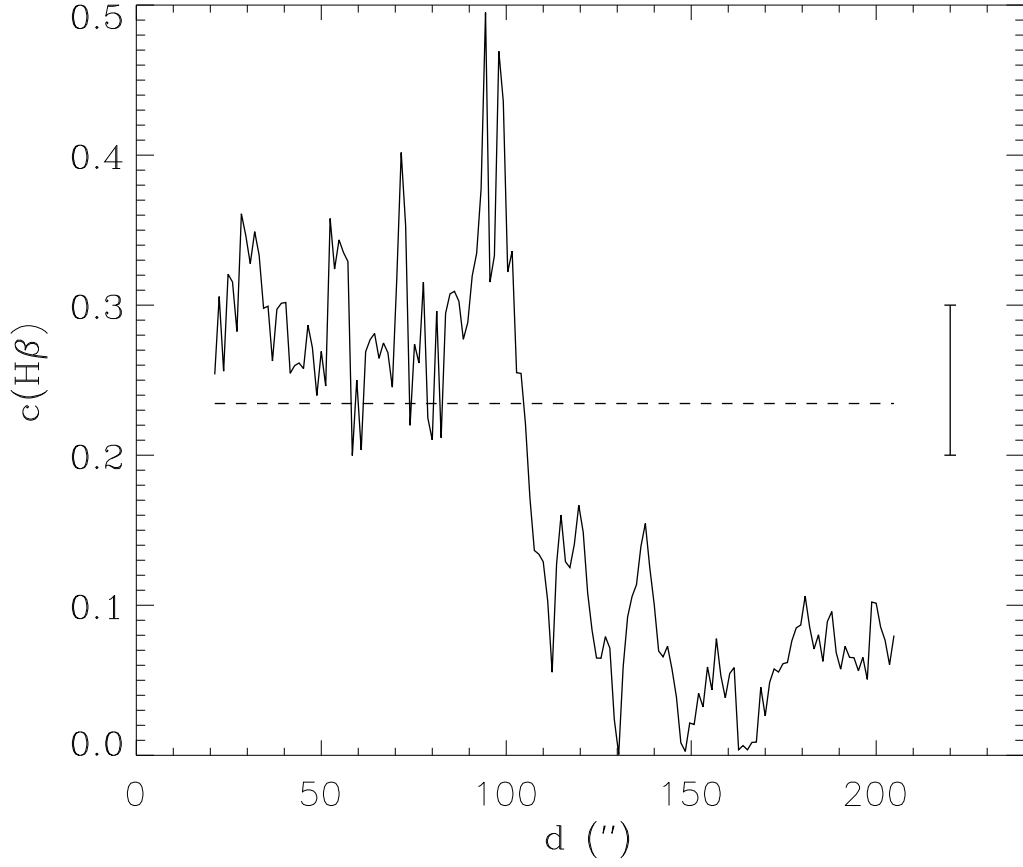


Fig. 2.— Spatial distribution of the reddening coefficient, $c(\text{H}\beta)$, along slit position 6. Positional measurement along the slit goes from northeast to southwest (see Figure 1). The dashed horizontal line represents the value of $c(\text{H}\beta)$ obtained from the integrated spectrum along the whole slit. The typical error bar is included.

ratios.

4.2. Ionic Abundances from CELs and RLs

Ionic abundances of N^+ , O^+ , O^{++} , S^+ , S^{++} , and Ar^{++} have been derived from CELs making use of the IRAF task *ionic* of the package *nebular*. We have assumed a two-zone scheme and $t^2 = 0$, adopting $T_e([N\ II])$ for ions with low ionization potential (N^+ , O^+ and S^+) and $T_e([O\ III])$ for ions with high ionization potential (O^{++} , S^{++} and Ar^{++}). The errors in the ionic abundances are the quadratic sum of the independent contributions of n_e , T_e , and line flux uncertainties.

On the other hand, the high signal-to-noise of the spectra has permitted us to detect and measure pure RLs of O II and C II in most of the apertures (see Figure 3). These lines have the advantage that their relative intensity with respect to H I lines depend weakly on T_e and n_e , avoiding the problem of the presence of temperature variations along the line of sight, that can actually affect the abundance determinations from CELs, which emissivities depend strongly on the T_e of the nebula.

Let $I(\lambda)$ be the intensity of a RL of a element X, i times ionized, at wavelength λ ; then the abundance of the ionization state $i + 1$ of element X is given by

$$\frac{N(X^{i+1})}{N(H^+)} = \frac{\lambda(\text{\AA})}{4861} \frac{\alpha_{eff}(H\beta)}{\alpha_{eff}(\lambda)} \frac{I(\lambda)}{I(H\beta)}, \quad (1)$$

where $\alpha_{eff}(\lambda)$ and $\alpha_{eff}(H\beta)$ are the effective recombination coefficients for the line and $H\beta$, respectively. The $\alpha_{eff}(H\beta)/\alpha_{eff}(\lambda)$ ratio is almost independent of the adopted temperatures and densities.

Following Esteban et al. (1998) we have considered the abundances obtained from the intensity of each individual line of multiplet 1 of O II and the abundances from the estimated total intensity of the multiplet. This last quantity is obtained by multiplying the sum of the intensities of the individual lines observed by the multiplet correction factor, defined as:

$$m_{cf} = \frac{\sum_{all} s_{ij}}{\sum_{obs} s_{ij}}, \quad (2)$$

where s_{ij} is the theoretical line strength, which are constructed assuming that they are proportional to the population of their parent levels assuming LTE computations predictions. The upper sum runs over *all* the lines of the multiplet and the lower sum runs over the *observed* lines of the multiplet.

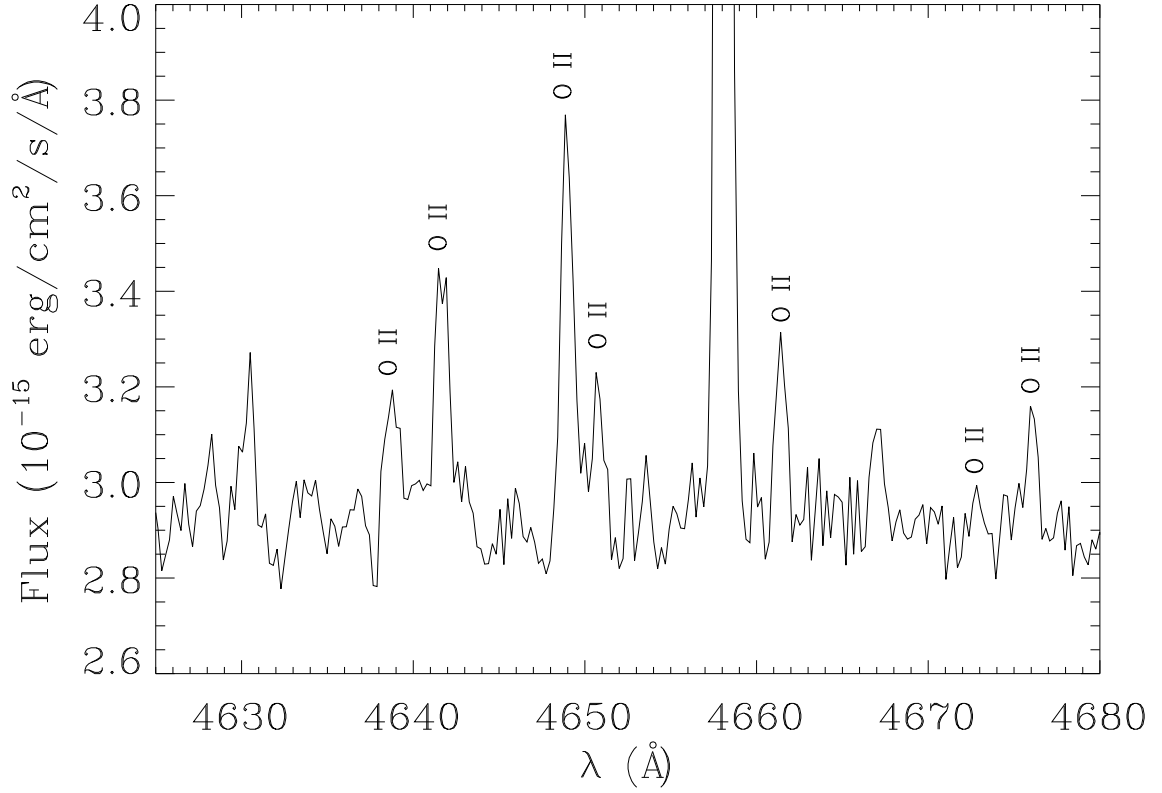


Fig. 3.— Portion of the blue spectrum of an aperture extracted from slit position 6 and extending from the positional measurements 151.4 to 152.6 arcseconds (see Figure 5). This is a representative example of the average quality of our 1D spectra.

The O^{++} and C^{++} abundances from RLs have been calculated using the representative T_e of these ions – $T_e([O\ III])$ – and the effective recombination coefficients available in the literature (Storey 1994 for $O\ II$ assuming LS coupling, and Davey, Storey, & Kisielius 2000 for $C\ II$). The O^{++} abundance has only been computed when at least three lines of multiplet 1 were measured in a given 1D spectrum. The final number of apertures with determinations of the O^{++}/H^+ ratio obtained from RLs was 671, a 92% of the total number of available 1D spectra. NLTE corrections are not taken into account for deriving the O^{++} abundances (see Tsamis et al. 2003; Ruiz et al. 2003; Peimbert et al. 2005) considering that we use several lines of the multiplet and the high densities –between 4000 and 6000 cm^{-3} (e.g. Esteban et al. 1998, 2004)– of the Orion nebula.

5. Spatial Profiles along the Slit Positions

5.1. Physical Conditions

The first step in the analysis of our results was the obtaining of spatial profiles of several nebular parameters along the slit positions. The selected parameters were: $c(H\beta)$, n_e , $T_e([N\ II])$, $T_e([O\ III])$, the intensity of several selected lines ($H\beta$, $C\ II\ 4267\ \text{\AA}$, $O\ II\ 4649\ \text{\AA}$, $[O\ III]\ 4959\ \text{\AA}$, $[Fe\ III]\ 4881\ \text{\AA}$, $[N\ II]\ 5755$ and $6584\ \text{\AA}$, $[O\ I]\ 6300\ \text{\AA}$, and $[S\ II]\ 6717 + 6731\ \text{\AA}$), the O^{++}/H^+ ratio obtained from CELs and RLs, and the C^{++}/H^+ ratio obtained from RLs. In figures 4 to 8 we show some selected spatial profiles of slit positions 3, 6, 1, 4, and 5, respectively. Slit positions 3 and 6 are the most interesting ones and we will focus our discussion on their main features. Slit position 3 crosses the Orion bar and the Herbig-Haro (H-H) objects HH 203 and HH 204 and slit position 6 passes through the brightest part of the nebula at the southwest of the Trapezium cluster, two proplyds: 159-350 and 177-341, and HH 530.

The spatial profiles of n_e show a large range of variation across the slits, with local maxima associated with the position of proplyds, H-H objects, the Orion bar, and the bright zone at the southwest of the Trapezium (see figures 4a to 8a). The highest densities are found at the proplyd 159-350 that has been observed in slit positions 5 and 6 (see figures 8a and 5a, respectively). This object shows n_e of the order of 6×10^4 and $2 \times 10^4\ cm^{-3}$ in positions 5 and 6, respectively; whereas the proplyd 158-326 –near $\theta^1\ Ori\ C$ – shows values somewhat larger than $4 \times 10^4\ cm^{-3}$ (See Figure 6a). The densities at the brightest zone of the nebula –the southwest of the Trapezium– are about $2.5 \times 10^4\ cm^{-3}$ (see Figure 5a). It is obvious that so high n_e determinations based on the $[S\ II]$ doublet are not totally confident because they are at the high-density limit of this indicator. The H-H objects are also associated with local peaks of n_e , but not as high as in the proplyds, in fact HH 202,

HH 203, and HH 204 show maxima between 6000 and $1 \times 10^4 \text{ cm}^{-3}$. In Figure 4a, the dashed line marks the n_e obtained from the “whole slit” (integrated) spectrum –2460 cm^{-3} – whereas the minimum and maximum values are about 700 and 8000 cm^{-3} , covering a range of one order of magnitude. In Figure 5a, we can see that the range of variation of n_e is also dramatic along slit position 6. In this figure we also compare the values corresponding to the “whole slit” spectrum –5500 cm^{-3} – and the “background gas” –4700 cm^{-3} – one, that corresponds to an integrated spectrum excluding the emission of the proplyds. As we can see, the measured density increases in 800 cm^{-3} –about a 17%– when we include the emission of the proplyds in the integrated spectrum of the slit.

The spatial profiles of $T_e([\text{N II}])$ and $T_e([\text{O III}])$ show very interesting features (see figures 4b to 8b). The proplyds observed in positions 1, 5, and 6 show quite prominent spikes of $T_e([\text{N II}])$ and lesser or almost absent ones of $T_e([\text{O III}])$. In slit position 6 (Figure 5b) the $T_e([\text{N II}])$ increases locally about 70% at proplyd 177-341, a similar spike shows 170-337 in slit position 5 (Figure 8b). The $T_e([\text{N II}])$ is also higher than the mean by 50% and 40% at the position of proplyd 159-250 in slit positions 5 and 6, respectively. In all the proplyds, the increase of $T_e([\text{O III}])$ is only of a few hundred K at most. In Figure 5b, we can also see a relatively broad –about 5'' wide– spike of $T_e([\text{N II}])$ at 130'', where the temperature increases about 15%. This feature is not related to any local structure reported by Bally et al. (2000) but with a conspicuous dark globule that can be seen at the edge of the bright zone at the southwest of the Trapezium. There are also less important temperature spikes related to some H-H objects. In Figure 4b, we can see that $T_e([\text{N II}])$ increases about 15% at HH 204 and that the increase is slightly lower in the case of $T_e([\text{O III}])$. In contrast, HH 203 do not show that behavior and its temperatures are similar to those of the surrounding gas. In HH 202 –slit position 4– the increase of $T_e([\text{N II}])$ and $T_e([\text{O III}])$ are only about 8% and 5%, respectively (Figure 7b). The other H-H objects we have observed –HH 529 and HH 530– do not show temperature variations with respect to the surrounding gas (figures 6b and 5b). The different behavior of the temperatures in the H-H objects does not seem to be correlated with the velocity of their associated flows as reported by Henney et al. (2007). There is a last interesting feature regarding the temperature profiles that can be seen in Figure 4b. Although $T_e([\text{N II}])$ is almost always a few hundred K larger than $T_e([\text{O III}])$ in all the slit positions (this has been also observed in previous works, e.g. Baldwin et al. 1991; Rubin et al. 2003), the zone around the Orion bar –between 130'' and 150'' in Figure 4b– shows a reversal of this relation just in the inner 10'' of the bar. In contrast, $T_e([\text{N II}])$ shows a local increase just outside the bar. This local increment of $T_e([\text{O III}])$ we see in this particular zone could be related with the highly ionized jet –specially bright in $[\text{O III}]$ – that leads to HH 203 and HH204 (see Doi et al. 2004). In fact, the position of this zone coincides with a knot of high $[\text{O III}]$ emission that can be seen in figure 8 of Doi et al. (2004) that is

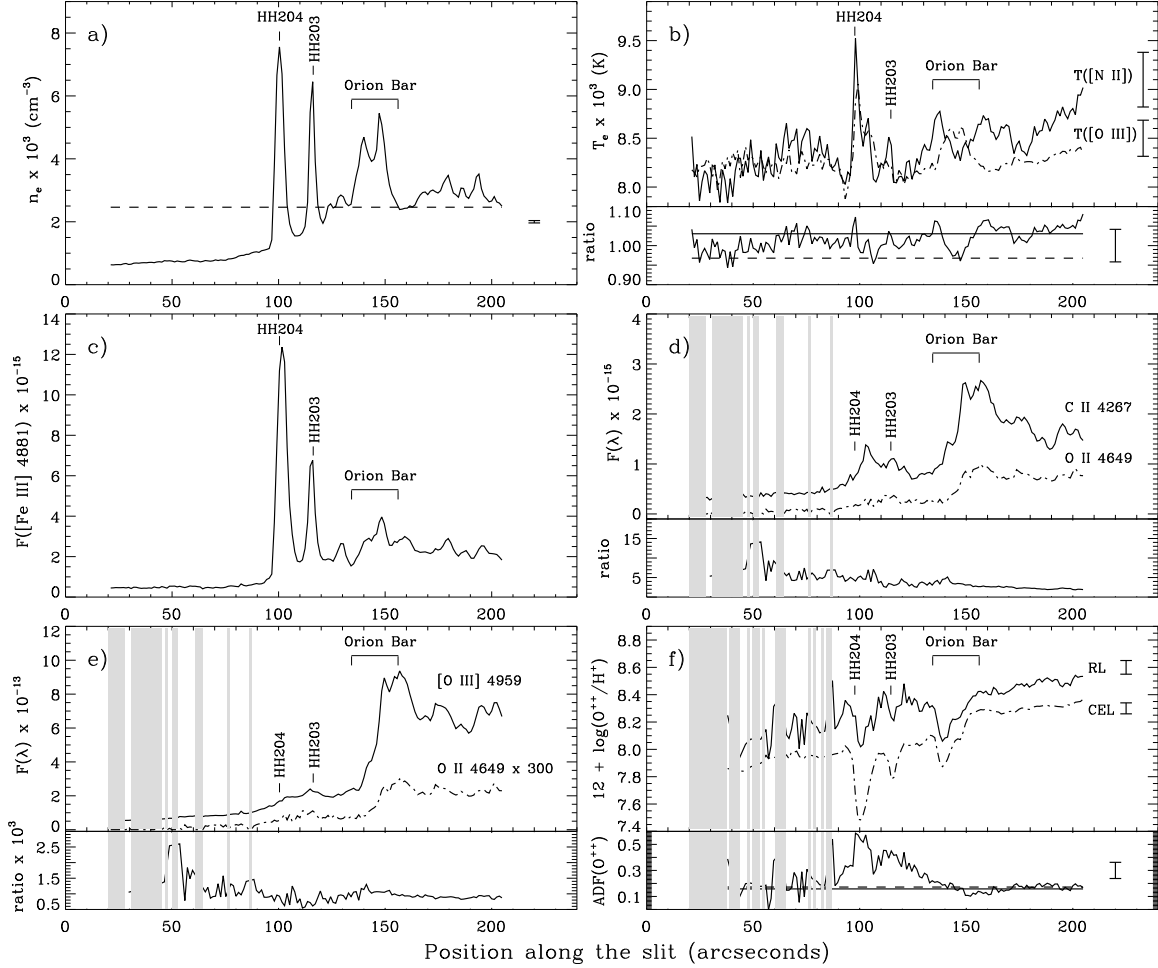


Fig. 4.— Spatial profiles of several nebular parameters along slit position 3. Positional measurement along the slit goes from southeast to northwest (see Figure 1). The position of the Orion bar and the Herbig-Haro objects HH 203 and HH 204 are indicated. Typical error bars are included in some of the diagrams. (a) n_e , the horizontal long-dashed line gives the average value of n_e for the “whole slit” (integrated) spectrum. (b) upper panel: $T_e([O\ III])$ (dashed-dotted line) and $T_e([N\ II])$ (continuous line); lower panel: $T_e([N\ II])/T_e([O\ III])$ ratio, the horizontal continuous and long-dashed lines represent the value of that ratio for the “background gas” and “whole slit” spectra, respectively. (c) $F([Fe\ III]\ 4881)$. (d) upper panel: $F(C\ II\ 4267)$ (continuous line) and $F(O\ II\ 4649)$ (dashed-dotted line); lower panel: $F(C\ II\ 4267)/F(O\ II\ 4649)$ ratio, the vertical grey lines indicate zones without a reliable measurement of the O II 4649 line. (e) upper panel: $F([O\ III]\ 4959)$ (continuous line) and $F(O\ II\ 4649)$ (dashed-dotted line), lower panel: $F([O\ III]\ 4959)/F(O\ II\ 4649)$ ratio, the vertical grey bands indicate zones without a reliable measurement of the O II 4649 line. (f) upper panel: $12 + \log(O^{++}/H^+)$ determined from RLs (continuous line) and CELs (dashed-dotted line); lower panel: $ADF(O^{++})$, the straight continuous and long-dashed lines represent the value of the ADF for the “background gas” and “whole slit” spectra, respectively, the vertical grey bands indicate zones without a reliable determination of the O^{++}/H^+ ratio from RLs.

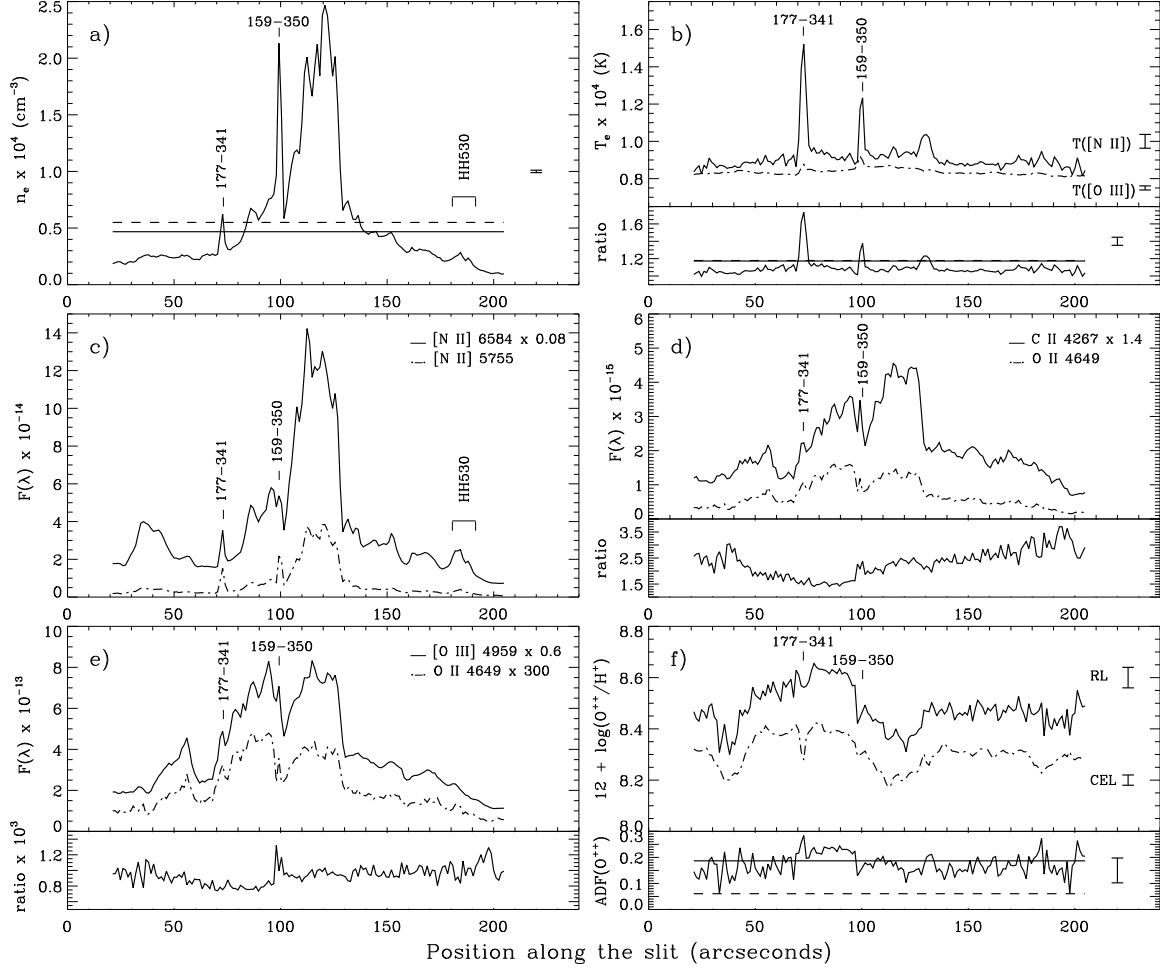


Fig. 5.— Spatial profiles of several nebular parameters along slit position 6. Positional measurement along the slit goes from northeast to southwest (see Figure 1). The position of the proplyds 177-341 and 159-350 and the Herbig-Haro object HH 530 are indicated. Typical error bars are included in some of the diagrams. (a) n_e , the horizontal continuous and long-dashed lines represent the value of n_e for the “background gas” and ‘whole slit’ spectra, respectively. (b) upper panel: $T_e([O\ III])$ (dashed-dotted line) and $T_e([N\ II])$ (continuous line); lower panel: $T_e([N\ II])/T_e([O\ III])$ ratio, the horizontal continuous and long-dashed lines represent the value of that ratio for the “background gas” and ‘whole slit’ spectra, respectively. (c) $F([N\ II]\ 5755)$ (continuous line) and $F([N\ II]\ 6584)$ (dashed-dotted line). (d) upper panel: $F(C\ II\ 4267)$ (continuous line) and $F(O\ II\ 4649)$ (dashed-dotted line); lower panel: $F(C\ II\ 4267)/F(O\ II\ 4649)$ ratio. (e) upper panel: $F([O\ III]\ 4959)$ (continuous line) and $F(O\ II\ 4649)$ (dashed-dotted line); lower panel: $F([O\ III]\ 4959)/F(O\ II\ 4649)$ ratio. (f) upper panel: $12 + \log(O^{++}/H^+)$ determined from RLs (continuous line) and CELs (dashed-dotted line); lower panel: $ADF(O^{++})$, the horizontal continuous and long-dashed lines represent the value of the ADF for the “background gas” and “whole slit” spectra, respectively.

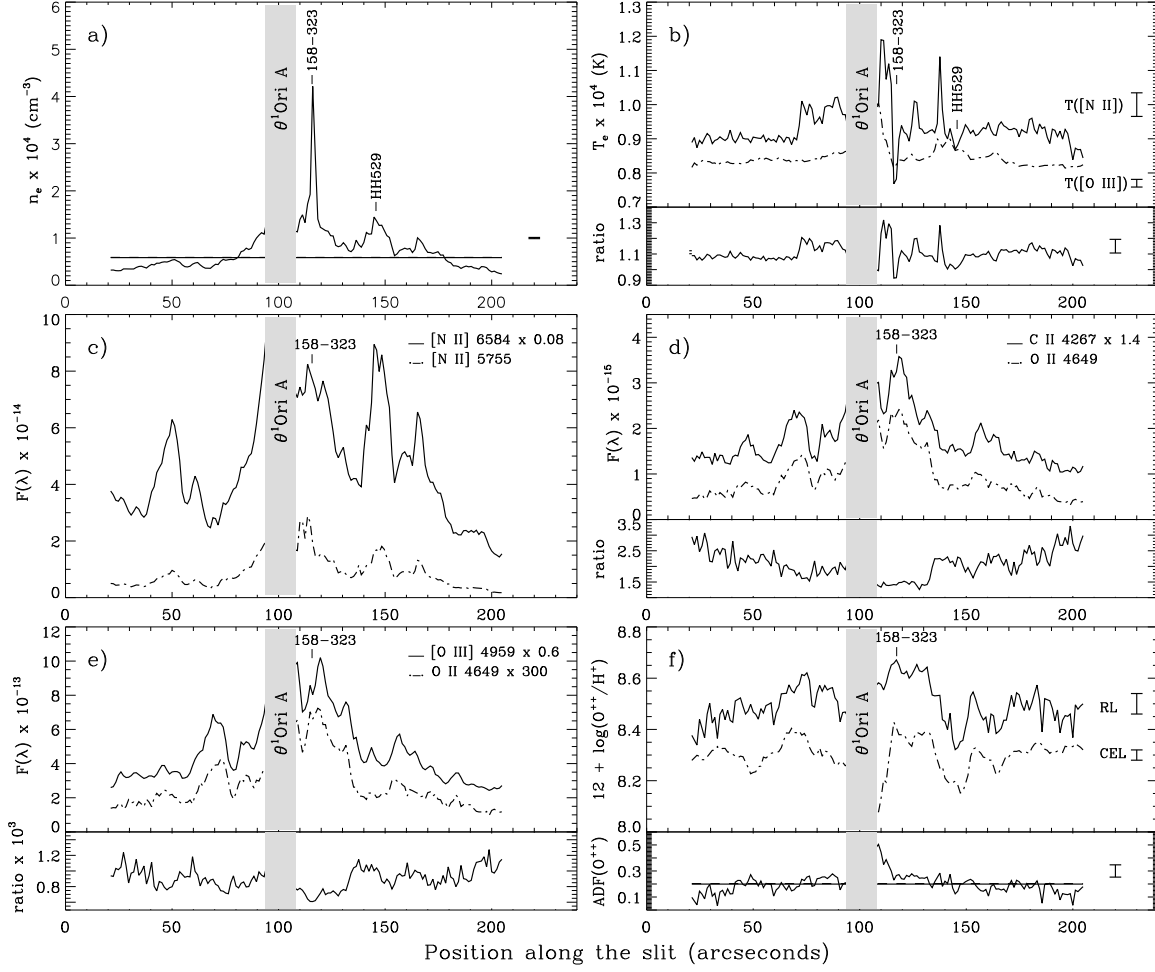


Fig. 6.— The same as Figure 5 but for slit position 1. Positional measurement along the slit goes from north to south (see Figure 1).

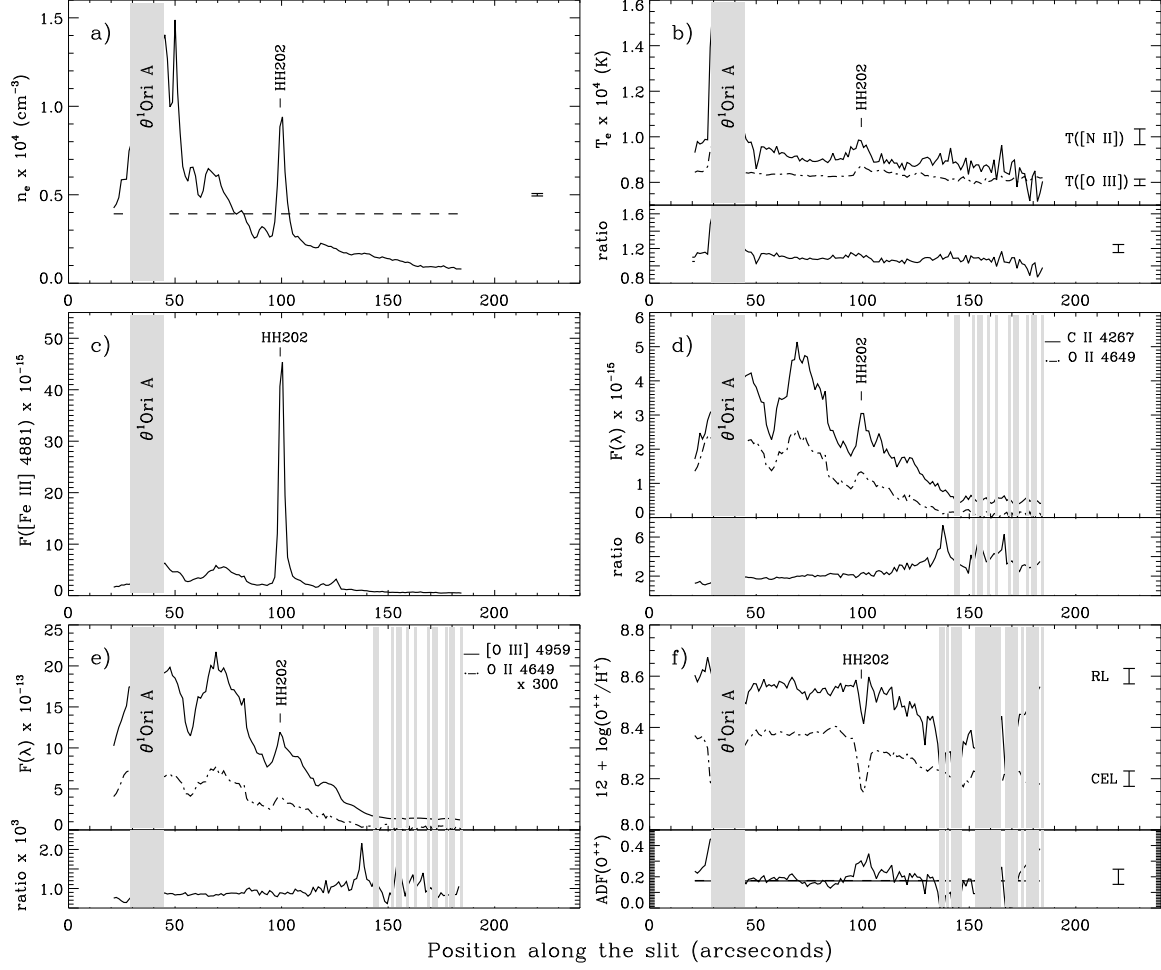


Fig. 7.— The same as Figure 4 but for slit position 4. Positional measurement along the slit goes from southeast to northwest (see Figure 1).

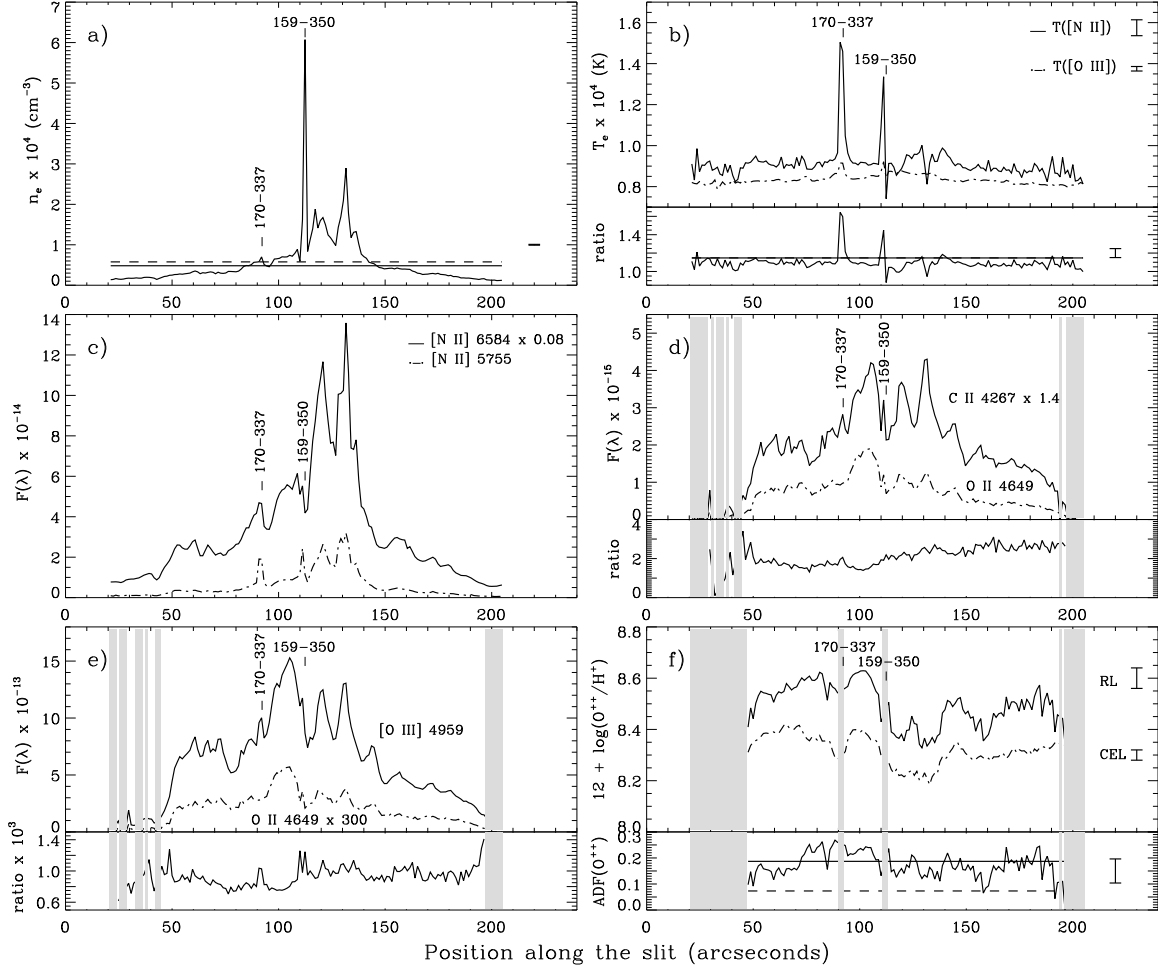


Fig. 8.— The same as Figure 5 but for slit position 5. Positional measurement along the slit goes from northeast to southwest (see Figure 1).

crossed by our slit (their box with the position-based identifier 209-446).

Rubin et al. (2003) obtained *HST*/STIS spectroscopy of a slit position very similar to our position 3 –their slit 4– and show its $T_e([\text{O III}])$ spatial profile in their figure 3a. If we compare that figure with our Figure 4b we can see that the point-to-point dispersion of the temperature is substantially lower in our data. In fact, whereas $T_e([\text{O III}])$ varies from 6500 to 12000 K in the slit 4 of Rubin et al. (2003) the variations are only from 8000 to 9000 K in our slit position 3. This fact has two possible explanations: a) the presence of real temperature variations with typical spatial scale between $0''.5$ (the spatial resolution of Rubin et al. data) and $1''.2$ (our resolution) in the plane of the sky, or b) the temperature variations reported by Rubin et al. (2003) are spurious and produced by the much lower signal-to-noise ratio of their data. We think that the second explanation is perhaps the most likely one considering that the deepest exposures obtained by Rubin et al. for the spectral range containing $[\text{O III}]$ 4363 Å were about 1060 s and our exposures were between 1800 and 2200 s long. Moreover, an important factor should be added due to the different apertures of the telescopes used in our and Rubin et al.’s datasets –4.2m and 2.4m, respectively– as well as the smallest element of spatial resolution used in Rubin et al.’s observations.

It is clear that the behavior of $T_e([\text{N II}])$ and $T_e([\text{O III}])$ at the positions of proplyds and H-H objects is different. In figures 4b to 8b we also include the ratio of both temperatures showing clearly that the increase of $T_e([\text{N II}])$ is higher than that of $T_e([\text{O III}])$ in proplyds. The presence of $T_e([\text{N II}])$ enhancements in the proplyds of the Orion nebula was previously reported by Rubin et al. (2003) and they interpret this as the effect of collisional deexcitation on the nebular lines of $[\text{N II}]$ due to the high densities of these objects. We have explored that possibility comparing the spatial profile of the intensity of $[\text{N II}]$ 5755 and 6584 Å lines. Both lines come from upper levels with very different critical densities – $7.9 \times 10^6 \text{ cm}^{-3}$ in the case of $[\text{N II}]$ 5755 Å line and $5.8 \times 10^4 \text{ cm}^{-3}$ in the case of $[\text{N II}]$ 6584 Å line. In figures 5c and 6c, we can see that the two proplyds with the largest electron densities ($n_e > 2.6 \times 10^4 \text{ cm}^{-3}$): 159-350 (also observed in Figure 8c) and 158-323 show a spike in the brightness of the $[\text{N II}]$ 5755 Å line, whereas the $[\text{N II}]$ 6584 Å line do not show a so clear increase in its brightness with respect to the emission of the surroundings. However, the proplyds showing the lowest electron densities ($n_e < 1 \times 10^4 \text{ cm}^{-3}$) 177-341 and 170-337 (figures 5c and 8c) show similar localized enhancements of the intensity of both $[\text{N II}]$ lines, indicating that collisional deexcitation seems to be not so important in these two proplyds.

In order to further explore if the different behavior of the auroral and nebular $T_e([\text{N II}])$ lines in some proplyds is due to collisional deexcitation, we have constructed Figure 9. In this figure, we show the theoretical curves of the n_e and T_e pairs that reproduce the observed range of values of the $[\text{N II}]$ 5755/6584 line ratio in the proplyds, as well as the line of the

lower limit of n_e corresponding to the lowest value of the [S II] 6731/6717 ratio measured in these objects. The theoretical predictions have been constructed with emissivities calculated by the photoionization code PHOTO as described in Stasińska (2005), gently provided by Grazyna Stasińska. Unfortunately, the results of Figure 9 are not conclusive, but considering that the estimated n_e of the proplyds should be a lower limit of the true one, the permitted area of the diagram indicates that collisional deexcitation should be acting. Moreover, if that is correct, the true electron temperature should be lower than that actually indicated by $T_e(\text{[N II]})$, but perhaps not too different that the values corresponding to the surrounding ionized gas (never lower than 3000 K). It is important to note that the $T_e(\text{[N II]})$ values we obtain for the “whole slit” and the “background gas” spectra of positions 5 and 6 only show differences of the order of a few ten K. This indicates that the contribution of proplyds in the integrated spectrum does not produce a substantial increase of the electron temperature derived. On the other hand, in contrast with what happens in proplyds, the increase of $T_e(\text{[N II]})$ that we see in H-H objects does not seem to be related to collisional deexcitation. This is suggested because the H-H objects show lower values of n_e and lower $T_e(\text{[N II]})$ peaks than the proplyds, their $T_e(\text{[N II]})$ and $T_e(\text{[O III]})$ show similar enhancements (see figures 4b and 7b), and the spatial coincidence of conspicuous similar peaks in both [N II] 5755 and 6584 Å lines. Therefore, the [N II] emission of the H-H objects should not be affected by substantial collisional deexcitation and their electron temperature is higher probably because the action of an additional source of heating, perhaps related to shock excitation.

5.2. Line Fluxes

One of the main spectral properties of H-H objects is their strong emission in [Fe III] lines. In Figure 4c, we can see the spatial profile of $F(\text{[Fe III] } 4881)/I(\text{H}\beta)$ line ratio along slit position 3. In HH 204, the intensity of that line is a factor 5 brighter than in the Orion bar. That object also shows a similar enhancement in the [O I] 6300 Å line and more moderate ones in the [S II] and [N II] lines. In the case of HH 202 –observed in slit position 4–, the intensity of [Fe III] 4881 Å line increases by a factor 10 (Figure 7c). The rest of the H-H observed: HH 204, HH 529, and HH 530 also show enhancements in [Fe III], [O I], [N II], and [S II] lines. These are common spectral features in shock-excited objects (see Hartigan et al. 1987). In contrast, the proplyds show [O I]⁴ spikes of moderate intensity and reversed spikes in the [S II] 6717, 6731 Å lines, perhaps also due to collisional deexcitation because of the rather low critical densities of the upper levels of those [S II] transitions. The

⁴The [O I] 6300 Å line could not be corrected from sky emission contribution. In any case, spatial variations of the intensity of this line along the slit can only be due to intrinsic nebular variations.

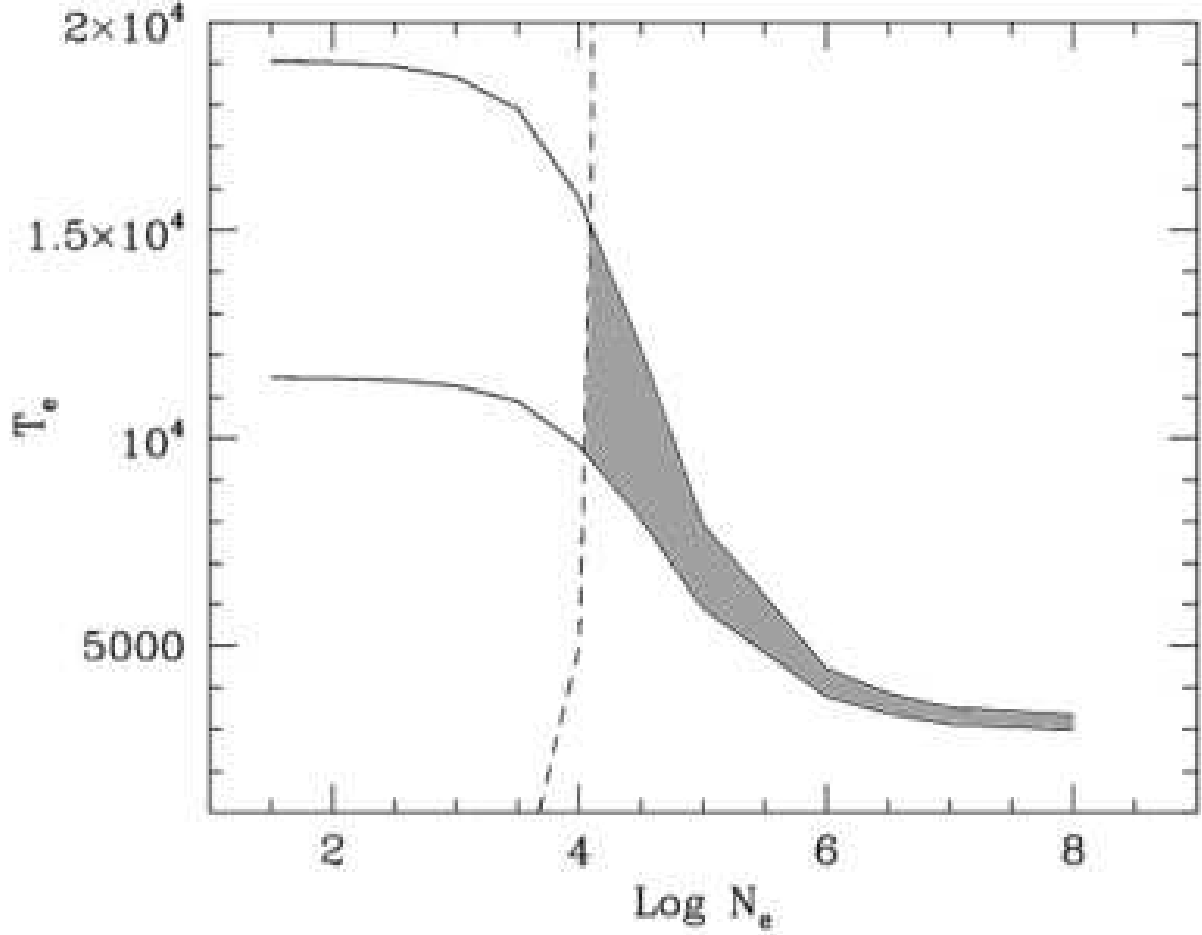


Fig. 9.— T_e vs. n_e . The continuous lines represent the theoretical curves of the n_e and T_e pairs that reproduce the observed range of values of the [N II] 5755/6584 line ratio measured in the proplyds. The dashed line represents the lower limit of the n_e corresponding to the lowest value of the [S II] 6731/6717 ratio measured in the proplyds. The grey area represents the permitted zone for the average spectral properties of the proplyds. The theoretical predictions have been constructed with emissivities calculated by the photoionization code PHOTO as described in Stasińska (2005), gently provided by Grazyna Stasińska.

[O I] emission emerges from the photodissociation of OH in the H/H₂ front that lies close to the protoplanetary disk surface (Storzer & Hollenbach 1998).

In figures 4d to 8d, we show the spatial profiles of the pure RLs of C II 4267 Å and O II 4649 Å along the slit positions. The spatial distribution of the C II and O II lines are very similar. However, in the cases of the slits positions passing through the center –specially in positions 1 and 6– there is a slight decrease of the C II/O II ratio towards the central parts of the nebula. This variation could be due to the increase of the C³⁺ ionization fraction near the Trapezium stars.

In figures 4e to 8e, we show the spatial profiles of the O II 4649 Å and [O III] 4959 Å lines, that show a fairly similar spatial distribution in all the slit positions. This behavior is very different to that observed in PNe (Liu et al. 2000; Garnett & Dinerstein 2001; Krabbe & Copetti 2006) where the O II line emission peaks closer to the central star than the [O III] line. We only find some localized enhancements of the [O III]/O II ratio, which are related to the position of some proplyds (see figures 5e and 8e). These enhancements of the [O III]/O II ratio are correlated with the increase of the continuum due to the emission of proplyds that show a large number of absorption features that produce a decrease in the intensity of the O II 4649 Å line (see §5.3).

5.3. The Abundance Discrepancy Factor

Finally, figures 4f to 8f show the spatial variation of the O⁺⁺/H⁺ ratios obtained from CELs and RLs as well as the AD factor, (hereinafter ADF) defined as:

$$\text{ADF}(\text{O}^{++}) = \log(\text{O}^{++}/\text{H}^+)_{\text{RLs}} - \log(\text{O}^{++}/\text{H}^+)_{\text{CELs}}, \quad (3)$$

for all the slit positions. The most interesting result concerning these figures is that the ADF remains fairly constant along most of the zones of the nebula observed, showing values between 0.15 and 0.20 dex, in agreement with the determinations by Esteban et al. (1998 and 2004) based on deep echelle spectrophotometry of selected small areas of the Orion nebula. It is necessary to note that the behavior of the ADF close to the proplyds is not confident because the O II lines are not properly measured in most of these objects due to the aforementioned strong increase of the continuum that makes difficult the measurement of weak lines and the effect of possible absorption features of their spectra. In any case, Figure 5f shows a quite convincing decrease of about 0.10 dex in the O⁺⁺/H⁺ ratios obtained from CELs at proplyd 177-341.

Another remarkable feature of the ADF along the slits can also be seen in Figure 5f, where we find a slightly higher ADF in an area between proplyds 159-350 and 177-341. It

is interesting to note that slit position 5 (Figure 8f) also shows the same higher values of the ADF between proplyd 159-350 and the area just at the north of 177-341. That common behavior in both slit positions indicates that the local increase of the ADF should be real. This enigmatic zone of relatively high ADF has an apparent diameter of about $30''$ and is located about $23''$ south of θ^1 Ori C star. There is not an apparent morphological and/or kinematical feature related to this zone.

In Figures 5f to 8f we also include the values of the ADF corresponding to the “whole slit” and the “background gas” spectra. It can be seen that the ADF of the “background gas” is consistent with the average value of the different individual apertures extracted from the slit positions. However, the ADF obtained for the “whole slit” spectrum –which is almost coincident with that of the “background gas” in slit position 1, 3, and 4– is substantially lower –about 0.1 dex– in slit positions 6 and 5 (figures 5f and 8f, respectively). The reason of this surprising result is most probably related to the strong contribution of the proplyds to the continuum of the integrated spectra and that this contribution is producing some absorption in the O II lines. In fact, in slit positions 5 and 6, the continuum adjacent to the O II 4649 Å line is about a factor 1.7 higher in the “whole slit” spectra than in the “background gas” one (see Figure 10 for slit position 5). This higher continuum is also associated with a decrease of the intensity ratios of O II lines with respect to $H\beta$. For example, the $I(\text{O II } 4649)/I(H\beta)$ ratio is about a 25% lower in the “whole slit” than in the “background gas” spectrum of slit position 6.

In figures 4f and 7f, we can note that the ADF is particularly large –reaching even values up to 0.6 dex– along HH 203, HH 204 and HH 202. The large increase of the ADF is due to the low values of the O^{++}/H^+ ratios determined by CELs in these zones. In contrast, the O^{++} abundances determined by RLs do not show so strong localized decrease. It is interesting to compare the behavior of the ADF at the H-H objects and at the Orion bar in Figure 4. In the bar, we can see a similar decrease of the O^{++}/H^+ ratios determined from both kinds of lines but producing an ADF similar to the mean value along the slit. As it has been discussed above, collisional deexcitation does not seem to affect the intensity of the nebular [N II] lines at HH 203 and HH 204 and, therefore, considering the larger critical densities of the [O III] lines, this effect is even less likely to be producing the observed decrease of the O^{++}/H^+ ratios determined from CELs. The observed behavior of the ADF in the H-H objects could be explained because the presence of a localized heating due to a non-radiative process –most likely shock excitation– that would lead to the derivation of a lower O^{++}/H^+ (CELs) ratio, and this seems to be the case for HH 204 that shows a conspicuous spike of $T_e([\text{O III}])$ (Figure 4b). However, this hypothesis fails to reproduce the presence of high ADFs in HH 203 and HH 202, where there are not spikes of $T_e([\text{O III}])$. Another explanation is the presence of a localized high t^2 in those particular zones but, unfortunately, we can not

check this possibility with our data. Finally, the other H-H objects observed –HH 529 and HH 530– do not show any distinguishable enhancement of the ADF.

6. Radial Distributions of Some Relevant Nebular Parameters

We have constructed radial distribution diagrams of several nebular parameters combining the data of the different slit positions and projecting the angular distance of the center of each individual 1D spectrum with respect to θ^1 Ori C (Figure 11). In these diagrams, we have only included the data of those apertures corresponding to the “background gas”, i.e. we have excluded all the points associated with proplyds or H-H objects. We include the same points in the three diagrams of Figure 11 and only those for which the ADF was calculated. These diagrams permit to study possible large scale variations of the properties of the ionized gas across the nebula.

In Figure 11a, we show the radial distribution of $T_e([\text{O III}])$, that shows a slight but clear general decrease with increasing distance from θ^1 Ori C. In this figure, it can be seen a bump in the temperature distribution of slit position 3 between $90''$ and $120''$. This bump corresponds to the local increase of $T_e([\text{O III}])$ that occurs at the inner part of the Orion bar (see also Figure 4b). We have made a least-squared linear fit to the data shown in Figure 11a but excluding those points belonging to the Orion bar. The result is:

$$T_e([\text{O III}])(\text{K}) = 8540 - 3.6 \times r, \quad (4)$$

where r is the distance from θ^1 Ori C in arcseconds. The uncertainty of the slope is $0.2 \text{ K arcsec}^{-1}$ and the Spearman’s correlation coefficient is 0.63 (hereinafter all the correlation coefficients we use are Spearman’s ones). Walter et al. (1992) obtained a radial distribution of $T_e([\text{O III}])$ with a positive slope of $6.7 \text{ K arcsec}^{-1}$ in the northwestern quadrant of the nebula, fitting their own data and other from the literature. The result of these authors disagrees with the clear behavior shown by our data in Figure 11a, that seems to be independent of the location of each slit position and even includes zones of the northwestern quadrant –our slit position 4. On the other hand, O’Dell et al. (2003) do not find significant spatial variations of $T_e([\text{O III}])$ across the nebula in their high-resolution map of the $[\text{O III}]$ ratio obtained with the WFPC at the *HST*. As we can see, the different results about the large-scale temperature variations in the Orion nebula are contradictory, however, we consider that our dataset is more reliable than the previous ones because it is based on homogeneous higher signal-to-noise ratio spectroscopic observations.

In Figure 11b, it is evident that $T_e([\text{N II}])$ also shows a radial decrease. The least-squared

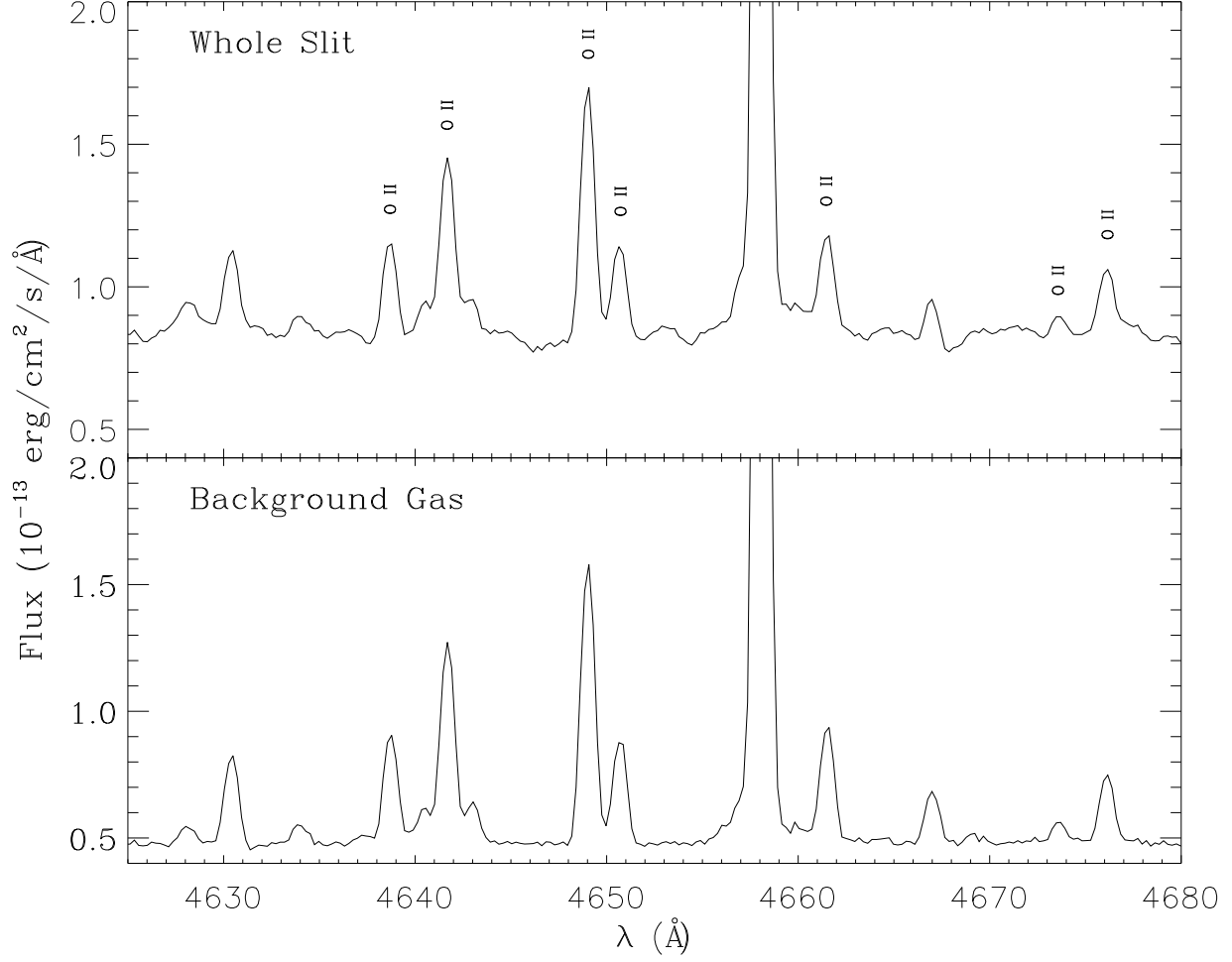


Fig. 10.— Comparison of the spectral area around the multiplet 1 of O II for the “whole slit” (up) and “background gas” (down) spectra of slit position 5. Note the rather different contribution of the continuum emission. The “whole slit” spectrum includes the emission of propyds and the “background gas” spectra do not.

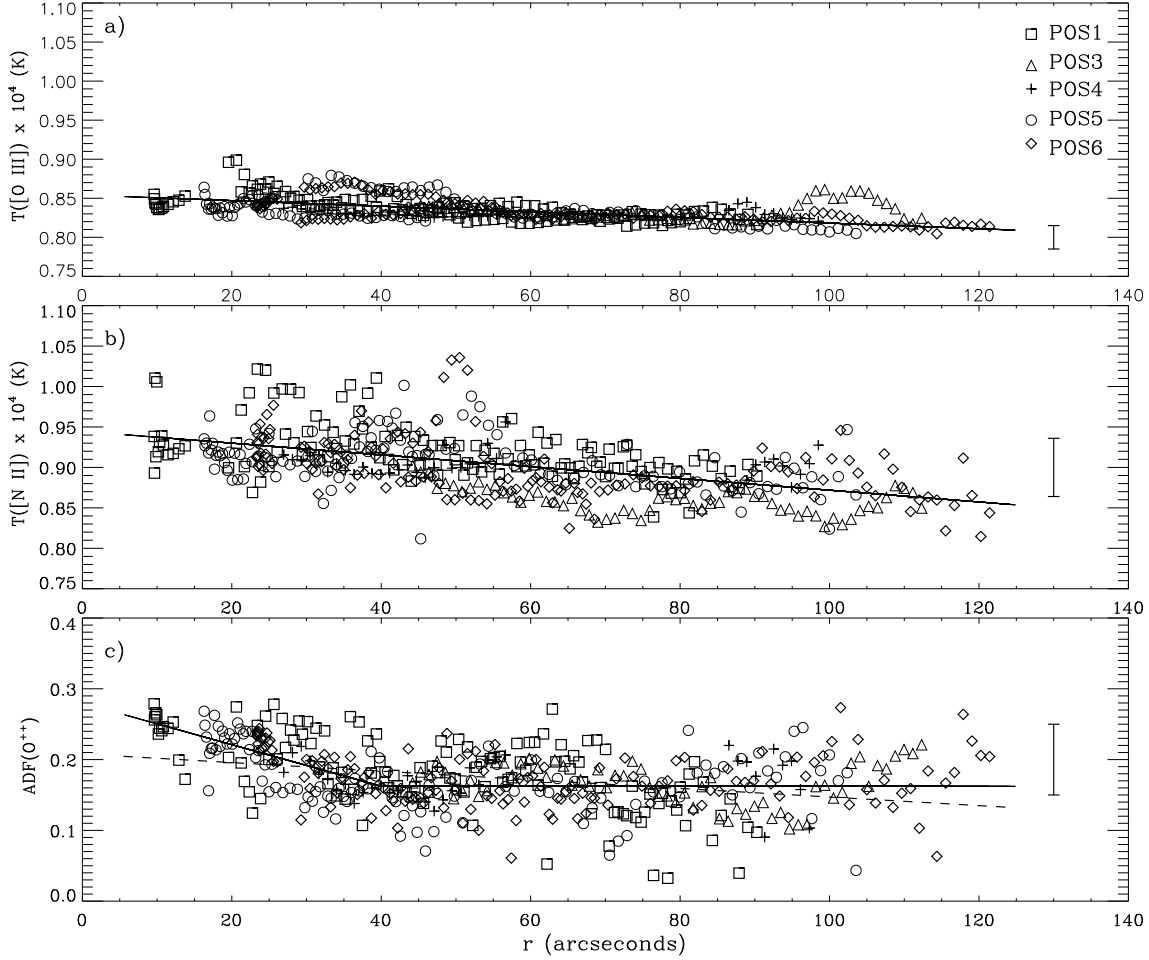


Fig. 11.— Radial distribution of the values of several nebular parameters along the Orion nebula. We have included the data of the apertures of all slit positions excluding those associated with proplyds or Herbig-Haro objects, i.e. the figures show the behavior of the featureless ionized gas. The abscissa axis indicates the projected angular distance of the center of each individual 1D spectrum with respect to θ^1 Ori C. Symbols are described in (a). Typical error bars are included in the different diagrams. (a) $T_e([\text{O III}])$, the continuous line represents a least-squared linear fit to the data. (b) $T_e([\text{N II}])$, the continuous line represents a least-squared linear fit to the data. (c) $\text{ADF}(\text{O}^{++})$, the dashed line represents a least-squared linear fit to the data, the continuous line represents a divided least-squared linear fit to the data into two regions inside and outside $40''$. The fits to the data are given in the text.

linear fit to the data gives:

$$T_e([\text{N II}])(\text{K}) = 9460 - 7.8 \times r . \quad (5)$$

We can see that the slope of the fit is larger than that obtained for $T_e([\text{O III}])$ and, in this case, the result agrees qualitatively with the temperature gradient obtained by Walter et al. (1992) from the $[\text{N II}]$ lines ($-17.1 \text{ K arcsec}^{-1}$) in the inner $170''$ of the nebula. The uncertainty of the slope of our fit is $0.6 \text{ K arcsec}^{-1}$ and its correlation coefficient is 0.52. Sánchez et al. (2007) obtain a bidimensional map of the spatial distribution of $T_e([\text{N II}])$ finding also that this parameter is higher near the Trapezium stars and drops towards the outer zones of the nebula, in qualitative agreement with our result.

Finally, in Figure 11c, we show the radial distribution of the $\text{ADF}(\text{O}^{++})$ across the nebula. In this figure, part of the relatively large dispersion is due to the large observation uncertainty in several apertures. In fact, most of the points with the highest and lowest values of the ADF correspond to low signal-to-noise ratio determinations at the edges of slit positions 1, 4, and 5. Despite the dispersion is relatively large, the first visual impression suggests that the ADF is rather constant or very slightly decreasing towards the outer parts of the nebula. In fact, the least-squares linear fit of all the points gives:

$$\text{ADF}(\text{O}^{++}) = 0.2050 - 0.0005 \times r , \quad (6)$$

but with a very low correlation coefficient (0.32). However, other possibilities of fitting are possible. A more detailed inspection of Figure 11c shows that the ADF seems to increase toward the center in the innermost $40''$ of the nebula and that this parameter becomes basically constant for larger distances (the inner points of slit positions 1 and 5 consistently suggest the same tendency). We have divided the least-squared linear fit to the ADF into two regions, the first for the points in the inner $40''$ and the second for the points outside this area –for which we have assumed a zero slope. The fits are the following:

$$\text{ADF}(\text{O}^{++}) = 0.279 - 0.003 \times r \quad (r \leq 40'') , \quad (7)$$

with a correlation coefficient of 0.58, and

$$\text{ADF}(\text{O}^{++}) = 0.163 \quad (r > 40'') . \quad (8)$$

This apparent increase of the ADF toward the inner zones of the nebula can be ultimately related to two other tendencies we have found in our data. Firstly, the clear correlation illustrated in Figure 11a showing that $T_e([\text{O III}])$ is higher in the zones near the Trapezium stars and, secondly, the possible weak correlation between the ADF and $T_e([\text{O III}])$ that will be discussed in §7. Therefore, the ADF seems to increase very slightly in the inner and

systematically hotter zones of the nebula. If this behavior is real, it would indicate that whatever process is producing the ADF it increases somehow with the local ionization of the gas or that it depends on the distance between θ^1 Ori C and the ionization front, from where most of the nebular emission comes. This last possibility arises because the blister geometry of the Orion nebula, the smaller distance of the Trapezium stars to the main ionization front occurs precisely behind that massive star cluster (see Wen & O’Dell 1995).

7. Correlations Between the ADF and Other Nebular Properties

In order to shed some light on the physical nature of the ADF problem, we have explored the relationship of this parameter with other nebular properties determined from our 1D spectra. Figure 12 illustrates the dependence of the ADF(O^{++}) with respect to a) $c(H\beta)$, b) n_e , c) $T_e([O\ III])$, d) $T_e([N\ II])/T_e([O\ III])$ ratio, e) O^{++} abundance determined from CELs, and f) O^{++}/O^+ ratio. As in Figure 11, we have only included the data of the apertures corresponding to the “background gas”. Figure 12a indicates that the ADF does not depend on the amount of dust present in the line of sight of each individual 1D spectrum. Also, there is no correlation between the ADF and n_e as it shown in Figure 12b. However, from this figure it would seem that ADFs larger than about 0.15 dex are only found in zones of $n_e < 1.3 \times 10^4\text{ cm}^{-3}$. This apparent trend is incidentally produced by the apertures of slit position 1, which are located near θ^1 Ori C and show the largest values of ADF, a behavior that does not seem to be related to n_e but perhaps with the increase of $T_e([O\ III])$, as we will see below. The large dispersion of the ADF for the lowest densities shown in Figure 12b is an observational bias. The less dense zones show the lowest surface brightnesses and therefore the faintest spectra, implying larger uncertainties in their ADF determinations. The behavior of the ADF with respect to $T_e([O\ III])$ is shown in Figure 12c and seems to show an apparent weak positive correlation, although $T_e([O\ III])$ shows a rather narrow interval of values in the nebula.

The other temperature indicator, $T_e([N\ II])$, shows a similar behavior and this is reflected in Figure 12d, where we represent the ADF versus the $T_e([N\ II])/T_e([O\ III])$ ratio. It is interesting to note that in Figure 12d the data points are distributed delineating the cloud of uncertainty around the average value of the ADF and $T_e([N\ II])/T_e([O\ III])$, illustrating that the portion of the nebula observed shows a tight proportionality between both quantities. The lack of correlation between the ADF and the ratio of electron temperatures of ions located in different zones of the nebula indicates that the natural temperature gradients that should exist in ionized nebulae –due to the different spatial location of the main nebular coolants– do not play a significant role in producing the observed ADF in the Orion nebula.

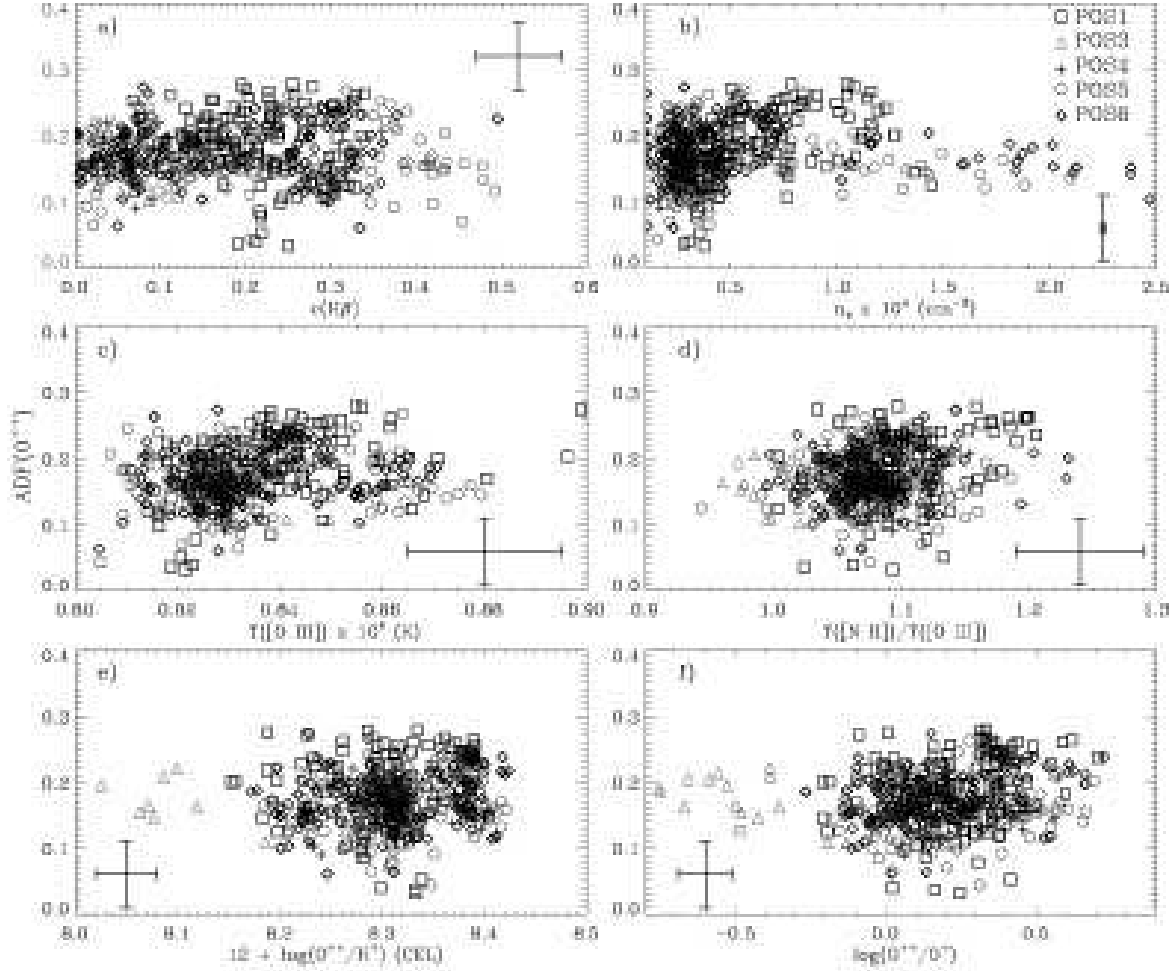


Fig. 12.— The abundance discrepancy factor of O^{++} , $ADF(O^{++})$, vs. several nebular parameters. We include the data from all slit positions. Symbols are described in (b). Typical error bars are included in the different diagrams. (a) $c(H\beta)$. (b) n_e . (c) $T_e([O\ III])$. (d) $T_e([N\ II])/T_e([O\ III])$ ratio. (e) O^{++} abundance determined from CELs. (f) O^{++}/O^+ ratio.

This results is consistent with that found by García-Rojas & Esteban (2007) in their analysis of integrated spectra of a sample of Galactic and extragalactic H II regions. Figure 12e also shows a lack of correlation between the ADF and the O^{++}/H^+ ratio obtained from CELs –a similar diagram is found in the case of the O^{++} abundance obtained from RLs, although the range of variation of the O^{++}/H^+ ratio is very narrow. Only the points belonging to the Orion bar show values of the O^{++} abundance between 0.2 and 0.3 dex lower than the typical ones of the rest of the nebula, but their corresponding ADF is similar. Finally, Figure 12f represents the behavior of the ADF with respect to the O^{++}/O^+ ratio and it is evident that, despite the relatively large range of values covered by the ionic ratio, there is not an apparent trend between both quantities.

8. Temperature Fluctuations

Following the formulation proposed by Peimbert (1967), the temperature fluctuation over the observed volume of a nebula can be parametrized in terms of the average temperature, T_0 , and the mean-square electron temperature fluctuation, t^2 , defined as:

$$T_0 = \frac{\int T_e n_e n_i dV}{\int n_e n_i dV} , \quad (9)$$

and

$$t^2 = \frac{\int (T_e - T_0)^2 n_e n_i dV}{T_0^2 \int n_e n_i dV} , \quad (10)$$

where n_i is the ion density. The integrations are calculated over the entire volume, and the element of volume, dV , can be expressed as $dl dA$, the product of the elements of length of column along the line of sight and surface area in the plane of the sky, respectively. Our spatially resolved spectroscopical data do not permit to obtain a direct determination of t^2 along the line of sight. However, a discrete estimation of t^2 in the plane of the sky – t_A^2 – can be obtained through the point-to-point determinations of the T_e we have obtained from the individual 1D spectra extracted along the slit positions. Following a similar procedure as Liu (1998), Rubin et al. (2003), and Krabbe & Copetti (2005) and assuming that $n_e \approx n(H^+)$ in all the points of the nebula, we can compute $T_{0,A}$ and t_A^2 using the following equations:

$$T_{0,A} = \frac{\sum_j T_{e,j} n_{e,j}^2 [n(X^{+i})/n(H^+)]_j}{\sum_j n_{e,j}^2 [n(X^{+i})/n(H^+)]_j} , \quad (11)$$

and

$$t_A^2 = \frac{\sum_j (T_{e,j} - T_{0,A})^2 n_{e,j}^2 [n(X^{+i})/n(H^+)]_j}{T_{0,A}^2 \sum_j n_{e,j}^2 [n(X^{+i})/n(H^+)]_j} , \quad (12)$$

where $T_{e,j}$, $n_{e,j}$, and $[n(X^{+i})/n(H^+)]_j$ are the electron temperature, electron density, and the ionic abundance of the X^{+i} species in the j -th aperture extracted from a given slit position. The $T_{e,j}$ used in the equations above corresponds to average temperatures along the line of sight that crosses the nebula at each j -th aperture and it can be expressed as:

$$T_{e,j} = \frac{\int T_e n_e n_i dl}{\int n_e n_i dl} . \quad (13)$$

Taking into account this fact, it is likely that the t_A^2 we obtain is substantially lower than t^2 and, more strictly speaking, it should be considered a lower limit to t^2 (see further argumentation given by Rubin et al. 2003; O’Dell et al. 2003). In Table 4, we summarize the values of t_A^2 we obtain for each slit position and for the two ions for which we have determinations of T_e . We have included all the points with T_e determination available in the sums, even those belonging to proplyds or H-H objects in order to explore the effect of these structures into the derivation of t^2 . Part of the value of t_A^2 we calculate for each ion comes from errors in the measurement of the emission line ratios, so the intrinsic t_A^2 must be corrected by the relative mean quadratic error of the T_e measurements, t_{Aer}^2 , with the simple relation $t_A^2 - t_{Aer}^2$ (see O’Dell et al. 2003; Krabbe & Copetti 2005). The values of t_{Aer}^2 for each ion and slit position are also included in Table 4 and are always lower than the corresponding t_A^2 except in the case of slit position 3, where the errors are slightly higher, indicating that most of the temperature variation along slit position 3 is produced by measurement uncertainties. The corrected t_A^2 we obtain is very low in all the cases, $t_A^2(O^{++})$ ranges from ~ 0 to 0.0011 and $t_A^2(N^+)$ from ~ 0 to 0.0112. However, Rubin et al. (2003) obtain $t_A^2(O^{++}) = 0.0068\text{--}0.0176$ and $t_A^2(N^+) = 0.0058\text{--}0.0175$ for the different slit positions they observe in the Orion nebula, values which are relatively consistent with ours in the case of $t_A^2(N^+)$ but considerably larger in the case of $t_A^2(O^{++})$. On the other hand, O’Dell et al. (2003) obtain $t_A^2(O^{++}) = 0.0050\text{--}0.0156$, values in good agreement with those obtained by Rubin et al. (2003) but also much higher than our determinations. The reason of this discrepancy is difficult to ascertain. The resolution element of each set of observations is rather different, our apertures are of $1''.2 \times 1''.03$, and those of Rubin et al. (2003) and O’Dell et al. (2003) are $0''.5 \times 0''.5$ and $0''.1 \times 0''.1$, respectively. If the spatial resolution has something to do with the different $t_A^2(O^{++})$ obtained by us and the previous works, this would imply that the small-scale spatial variations of $T_e([O\ III])$ have a characteristic size between $0''.5$ and $1''.0$ and that those related to $T_e([N\ II])$ are larger, at least of the order of the size of our apertures. In any case, this seems to us a rather unlikely scenario. Another difference between our determinations and those of Rubin et al. (2003) and O’Dell et al. (2003) is that those authors use a relation for determining T_e from the $[O\ III]$ line ratio that is valid in the low-density limit, while our calculations are based on the solving of the statistical equilibrium equations for the n_e measured for each particular aperture. We have explored the effect of this different

procedure applying equation 5 of Rubin et al. (2003) –also used by O’Dell et al. (2003)– to our data of slit position 6. In Figure 13, we show the ratio of the $T_e([O\ III])$ computed using the low-density limit approximation equation and our own determinations finding a systematical bias of about 1.12 and a small bump ($\sim 5\%$) coincident with the zone of the highest density at the southwest of the Trapezium (see Figure 5a). The use of both different procedures do not substantially increase the T_e dispersion. In fact, using the low-density limit approximation, we obtain $t_A^2(O^{++}) = 0.0008$ for slit position 6, only 60% larger than our calculations. Therefore, the use of a low-density limit approximation does not explain the large differences of $t_A^2(O^{++})$ find by us and the other authors. A last possibility is the different signal-to-noise ratio of the datasets we are comparing. As it was commented in § 5.1, this is a likely source of discrepancy in the case of the long-slit data of Rubin et al. (2003), but this is more difficult to ascertain in the case of the data of O’Dell et al. (2003). These authors estimate a representative probable error of about 4.2% for their point-to-point $T_e([O\ III])$ determinations, which corresponds to a t_{Aer}^2 of about 0.0017, larger than our observational errors, but much lower than their nominal values of $t_A^2(O^{++})$, indicating that the temperature variations obtained by O’Dell et al. (2003) should be real if the errors are not largely underestimated. Only observations combining very high signal-to-noise ratio and very high spatial resolution would ascertain this puzzle.

As it has been stated before, our spatially-resolved spectroscopical data do not permit to determine t^2 along the line of sight –that we will denote as t_l^2 – but an indirect estimate can be obtained assuming that the ADF is produced by the presence of such temperature variations. Although this is still a controversial possibility, there are some pieces of evidence indicating that this may be correct, at least in the case of H II regions (see García-Rojas & Esteban 2007). O’Dell et al. (2003) show that the relation between t_A^2 , t_l^2 , and the total t^2 in three dimensions is:

$$t^2 = t_A^2 + \langle t_l^2 \rangle , \quad (14)$$

where $\langle t_l^2 \rangle$ is the average over all lines of sight. In Table 4, we include the $\langle t_l^2(O^{++}) \rangle$ we obtain for each slit position. These values have been estimated from the average ADF(O^{++}) of the individual apertures of each slit position. From the table, it can be seen that the $\langle t_l^2(O^{++}) \rangle$ is rather similar for the different slit positions and consistent with previous determinations –between 0.018 and 0.028 (Esteban et al. 1998, 2004)– except in the case of slit position 3, that shows a rather higher value. This large temperature fluctuation comes from the also larger ADFs we obtain at HH 203 and HH 204 (see Figure 4f). Taking into account that the values of $t_A^2(O^{++})$ are much lower than $\langle t_l^2(O^{++}) \rangle$, it can be considered that $t^2(O^{++}) \approx \langle t_l^2(O^{++}) \rangle$. Following the argumentation of O’Dell et al. (2003), this result would indicate that the hypothetical thermal inhomogeneities producing t^2 should be small-scale ones and unresolved by our data, i.e. smaller than our spatial resolution limit of about

Table 3. Selected lines

λ (Å)	Ion	Mult.	λ (Å)	Ion	Mult.
4267.15	C II	6	5517.71	[Cl III]	1F
4340.47	H I	H γ	5537.88	[Cl III]	1F
4363.21	[O III]	2F	5754.64	[N II]	3F
4638.86	O II	1	6300.30	[O I]	1F
4640.64	N III	2	6312.10	[S III]	3F
4641.81	O II	1	6363.78	[O I]	1F
4643.06	N II	5	6548.03	[N II]	1F
4649.13	O II	1	6562.82	H I	H α
4650.84	O II	1	6583.41	[N II]	1F
4661.63	O II	1	6716.47	[S II]	2F
4711.37	[Ar IV]	1F	6730.85	[S II]	2F
4861.33	H I	H β	7135.78	[Ar III]	1F
4881.00	[Fe III]	2F	7319.19	[O II]	2F
4958.91	[O III]	1F	7330.20	[O II]	2F
5006.94	[O III]	1F	7751.10	[Ar III]	2F

Table 4. Values of t_A^2 , t_{Aer}^2 , and t_l^2

Slit Position	$t_A^2(\text{O}^{++})$	$t_{Aer}^2(\text{O}^{++})$	$t_A^2(\text{N}^+)$	$t_{Aer}^2(\text{N}^+)$	$\langle t_l^2(\text{O}^{++}) \rangle$
1	0.0013	0.0002	0.0127	0.0015	0.028
3	0.0004	0.0006	0.0010	0.0011	0.038
4	0.0008	0.0003	0.0055	0.0016	0.029
5	0.0004	0.0002	0.0126	0.0019	0.025
6	0.0005	0.0002	0.0024	0.0017	0.025

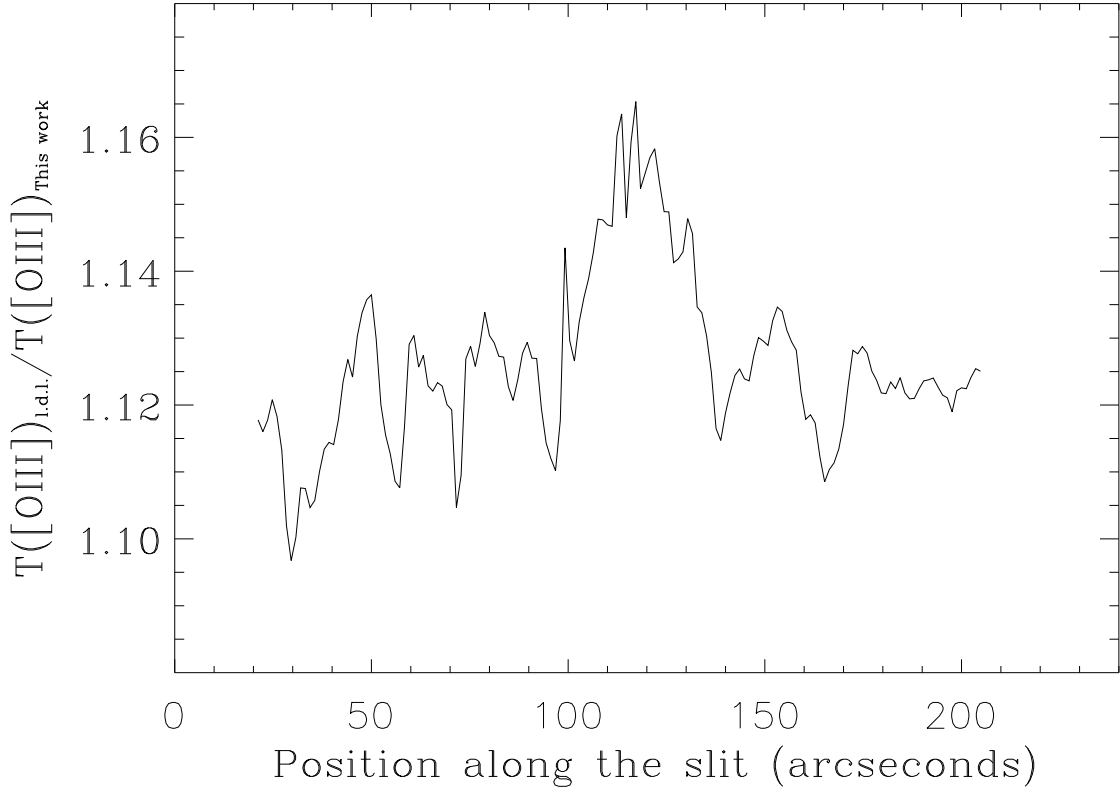


Fig. 13.— Ratio of the $T_e([\text{O III}])$ computed using the low-density limit (l.d.l.) approximation equation used by Rubin et al. (2003) and our own determinations along slit position 6. Positional measurement along the slit goes from northeast to southwest (see Figure 1).

1". On the other hand, our spatial resolution is unable to resolve the size of 10^{13} – 10^{15} cm that Stasińska et al. (2007) derive for the metal-rich droplets they claim to be the most likely explanation of the AD.

9. Conclusions

We have studied the spatial distribution of a large number of nebular quantities along five slit positions covering different morphological zones of the Orion nebula. The resolution element of the observations was $1''.2 \times 1''.03$. The studied quantities were $c(\text{H}\beta)$, n_e , $T_e([\text{N II}])$, $T_e([\text{O III}])$, the intensity of several selected lines ($\text{H}\beta$, $\text{C II } 4267 \text{ \AA}$, $\text{O II } 4649 \text{ \AA}$, $[\text{O III}] 4959 \text{ \AA}$, $[\text{Fe III}] 4881 \text{ \AA}$, $[\text{N II}] 5755$ and 6584 \AA , $[\text{O I}] 6300 \text{ \AA}$, and $[\text{S II}] 6717 + 6731 \text{ \AA}$), the O^{++}/H^+ ratio obtained from collisionally excited lines (CELs) and recombination lines (RLs), and the C^{++}/H^+ ratio obtained from RLs. The total number of apertures or 1D spectra extracted was 730. We have been able to determine the O^{++}/H^+ ratio from the faint RLs of this ion in a 92% of the apertures.

The spatial distribution of n_e shows a large range of variation –larger than an order of magnitude– across the nebula, with local maxima associated with the position of protoplanetary disks (proplyds), Herbig-Haro objects, the Orion bar, and the brightest area of the nebula at the southwest of the Trapezium. The proplyds show quite prominent spikes of $T_e([\text{N II}])$ and much lesser ones of $T_e([\text{O III}])$. This fact could be due to collisional deexcitation on the nebular lines of $[\text{N II}]$ because of the high densities of these objects. Herbig-Haro objects also show somewhat higher values of $T_e([\text{N II}])$ but, in this case, the origin could be related to extra heating of the gas due to shock excitation. The spatial distribution of the $\text{O II } 4949 \text{ \AA}$ and $[\text{O III}] 4959 \text{ \AA}$ lines is fairly similar along all the slit positions, a very different behavior to that observed in planetary nebulae. We have found that the abundance discrepancy factor (ADF) of O^{++} –the difference between the O^{++} abundance determined from RLs and CELs– remains, in general, rather constant along most of the observed areas of the nebula, showing values between 0.15 and 0.20 dex. However, there are some localized enhancements of the ADF, specially at the position of the Herbig-Haro objects HH 202, HH 203, and HH 204.

The combined data of all slit positions indicate a clear decrease of $T_e([\text{N II}])$ and $T_e([\text{O III}])$ with increasing distance from the main ionizing source of the nebula, $\theta^1 \text{ Ori C}$. On the other hand, the radial distribution of the ADF shows a rather constant value across the nebula except at the inner $40''$, where the ADF seems to increase very slightly toward $\theta^1 \text{ Ori C}$.

We have explored possible correlations between the ADF of O^{++} and other nebular quantities, finding a possible very weak increase of the ADF for higher electron temperatures. There are not apparent trends between the ADF and $c(H\beta)$, n_e , the $T_e([N\ II])/T_e([O\ III])$ ratio, O^{++} abundance, and the O^{++}/O^+ ratio.

Our spatially resolved spectroscopy allows to estimate the value of the mean-square electron temperature fluctuation in the plane of the sky, a lower limit to the traditional t^2 parameter. We find very low values in all cases, result that is in contradiction with previous estimates from the literature. Our results indicate that the hypothetical thermal inhomogeneities –if they exist– should be lower than our spatial resolution limit of about $1''$.

It is clear that further studies on the T_e , chemical abundances, and ADF distributions at sub-arcsec spatial scales are necessary in trying to disentangle (a) whether small spatial scale temperature fluctuations and/or metal-rich droplets are really present in the Orion nebula and HII regions in general, and (b) the origin of AD problem and its possible relation with t^2 and other nebular properties. The observations needed for this task are very difficult even for ground-based large-aperture telescopes and, by now, unfeasible with the current space telescopes and their available instrumentation.

We thank G. Stasińska and M. Rodríguez for their fruitful comments and help. We are grateful to the referee, Y. Tsamis, for his careful reading of the paper and his comments. This work has been funded by the Spanish Ministerio de Ciencia y Tecnología (MCyT) under project AYA2004-07466.

REFERENCES

- Baldwin, J. A., Ferland, G. J., Martin, P. G., Corbin, M. R., Cota, S. A., Peterson, B. M., & Slettebak, A. 1991, *ApJ*, 374, 580
- Bally, J., O’Dell, C. R., & McCaughrean, M. J. 2000, *AJ*, 119, 2919
- Castañeda, H. O., Vilchez, J. M., & Copetti, M. V. F. 1992, *A&A*, 260, 370
- Castellanos, M., Díaz, A. I., & Terlevich, E. 2002, *MNRAS*, 329, 315
- Costero, R., & Peimbert, M. 1970, *Boletín de los Observatorios Tonantzintla y Tacubaya*, 5, 229
- Davey, A. R., Storey, P. J., & Kisieliński, R. 2000, *A&AS*, 142, 85
- Doi, T., O’Dell, C. R., & Hartigan, P. 2004, *AJ*, 127, 3456

- Esteban, C., García-Rojas, J., Peimbert, M., Peimbert, A., Ruiz, M. T., Rodríguez, M., & Carigi, L. 2005, *ApJ*, 618, L95
- Esteban, C., Peimbert, M., García-Rojas, J., Ruiz, M. T., Peimbert, A., & Rodríguez, M. 2004, *MNRAS*, 355, 229
- Esteban, C., Peimbert, M., Torres-Peimbert, S., & Escalante, V. 1998, *MNRAS*, 295, 401
- Esteban, C., Peimbert, M., Torres-Peimbert, S., & Rodríguez, M. 2002, *ApJ*, 581, 241
- French, H. B. 1983, *ApJ*, 273, 214
- García-Rojas, J. 2006, PhD thesis, Universidad de La Laguna
- García-Rojas, J., & Esteban, C. 2007, ArXiv e-prints, 0707.3518
- García-Rojas, J., Esteban, C., Peimbert, A., Peimbert, M., Rodríguez, M., & Ruiz, M. T. 2005, *MNRAS*, 362, 301
- García-Rojas, J., Esteban, C., Peimbert, A., Rodríguez, M., Peimbert, M., & Ruiz, M. T. 2007, *Rev. Mexicana Astron. Astrofis.*, 43, 3
- García-Rojas, J., Esteban, C., Peimbert, M., Costado, M. T., Rodríguez, M., Peimbert, A., & Ruiz, M. T. 2006, *MNRAS*, 368, 253
- García-Rojas, J., Esteban, C., Peimbert, M., Rodríguez, M., Ruiz, M. T., & Peimbert, A. 2004, *ApJS*, 153, 501
- Garnett, D. R., & Dinerstein, H. L. 2001, *ApJ*, 558, 145
- Hartigan, P., Raymond, J., & Hartmann, L. 1987, *ApJ*, 316, 323
- Henney, W. J., O'Dell, C. R., Zapata, L. A., García-Díaz, M. T., Rodríguez, L. F., & Robberto, M. 2007, *AJ*, 133, 2192
- Krabbe, A. C., & Copetti, M. V. F. 2005, *A&A*, 443, 981
- . 2006, *A&A*, 450, 159
- Liu, X.-W. 1998, *MNRAS*, 295, 699
- Liu, X.-W., Storey, P. J., Barlow, M. J., Danziger, I. J., Cohen, M., & Bryce, M. 2000, *MNRAS*, 312, 585

- López-Sánchez, A. R., Esteban, C., García-Rojas, J., Peimbert, M., & Rodríguez, M. 2007, *ApJ*, 656, 168
- Mathis, J. S., & Liu, X.-W. 1999, *ApJ*, 521, 212
- O’Dell, C. R. 2001, *PASP*, 113, 29
- O’Dell, C. R., Peimbert, M., & Peimbert, A. 2003, *AJ*, 125, 2590
- O’Dell, C. R., & Wong, K. 1996, *AJ*, 111, 846
- O’Dell, C. R., & Yusef-Zadeh, F. 2000, *AJ*, 120, 382
- Osterbrock, D. E., & Ferland, G. J. 2006, *Astrophysics of gaseous nebulae and active galactic nuclei* (2nd. ed. Sausalito, CA: University Science Books)
- Peimbert, A., Peimbert, M., & Ruiz, M. T. 2005, *ApJ*, 634, 1056
- Peimbert, M. 1967, *ApJ*, 150, 825
- Peimbert, M., Storey, P. J., & Torres-Peimbert, S. 1993, *ApJ*, 414, 626
- Pogge, R. W., Owen, J. M., & Atwood, B. 1992, *ApJ*, 399, 147
- Rola, C., & Stasińska, G. 1994, *A&A*, 282, 199
- Rubin, R. H., Martin, P. G., Dufour, R. J., Ferland, G. J., Blagrove, K. P. M., Liu, X.-W., Nguyen, J. F., & Baldwin, J. A. 2003, *MNRAS*, 340, 362
- Ruiz, M. T., Peimbert, A., Peimbert, M., & Esteban, C. 2003, *ApJ*, 595, 247
- Sánchez, S. F., Cardiel, N., Verheijen, M. A. W., Martín-Gordón, D., Vilchez, J. M., & Alves, J. 2007, *A&A*, 465, 207
- Shaw, R. A., & Dufour, R. J. 1995, *PASP*, 107, 896
- Stasińska, G. 2005, *A&A*, 434, 507
- Stasińska, G., Tenorio-Tagle, G., Rodríguez, M., & Henney, W. J. 2007, *A&A*, 471, 193
- Storey, P. J. 1994, *A&A*, 282, 999
- Storey, P. J., & Hummer, D. G. 1995, *MNRAS*, 272, 41
- Storzer, H., & Hollenbach, D. 1998, *ApJ*, 502, L71

Tsamis, Y. G., Barlow, M. J., Liu, X.-W., Danziger, I. J., & Storey, P. J. 2003, MNRAS, 338, 687

Tsamis, Y. G., & Péquignot, D. 2005, MNRAS, 364, 687

Walter, D. K., Dufour, R. J., & Hester, J. J. 1992, ApJ, 397, 196

Wen, Z., & O’Dell, C. R. 1995, ApJ, 438, 784